Materials Advances

ROYAL SOCIETY OF CHEMISTRY

REVIEW

View Article Online
View Journal | View Issue

Open Access Article. Published on 25 agosto 2023. Downloaded on 8/8/2025 16:09:06.
This article is licensed under a Creative Commons Attribution 3.0 Unported Licence.

Check for updates

Cite this: *Mater. Adv.*, 2023, 4, 3989

MXene and their integrated composite-based acetone sensors for monitoring of diabetes

Monu Gupta, Arpit Verma, Priyanka Chaudhary and B. C. Yadav *

For present-day technological advancements, the MXene family is a highly investigated material in the family of van der Waals heterostructures. MXenes possess exceptional physical, optical, electrical, and electronic properties. Herein, their vast electroactive surfaces, MXene-based sensors and their integration with other materials for enhanced sensing performance are discussed. The challenges and future directions of MXene-based VOCs sensors are also considered. This review emphasizes the potential of MXene in addressing environmental and health-related concerns, particularly in acetone sensing. Acetone, a volatile organic compound (VOC), is dangerous due to its explosiveness and toxicity, causing various health issues. Detecting acetone gas has medical and environmental applications, including diabetes diagnosis and environmental monitoring. This review aims to analyze recent advancements in chemiresistive sensors for acetone gas detection using MXene and MXene composite materials, discussing the synthesis methods, characterization, response and recovery time, and sensing mechanisms to achieve further improvements in sensor performance. The average amount of acetone detected in the breath of healthy people is less than 1 ppm (0.3–0.9 ppm), but it increases to 2.2 and 1.7 ppm in type 1 and type 2 diabetic patients, respectively. As a result, the ability to recognize acetone concentrations at levels sub-ppm, or even at ppb levels, is crucial for the early detection of diabetes. Nowadays, breath analysis has attracted much attention as a potentially powerful tool for studying medical diagnosis diseases due to its noninvasive nature and real-time monitoring ability. In VOCs, acetone is considered to be an important breath biomarker for diabetes.

Received 21st April 2023,
Accepted 7th August 2023

DOI: 10.1039/d3ma00188a

rsc.li/materials-advances

Nanomaterials and Sensors Research Laboratory, Department of Physics, School of Physical and Decision Science, Babasaheb Bhimrao Ambedkar University, Lucknow-226025, India. E-mail: balchandra_yadav@rediffmail.com

1. Introduction

MXene and its associated nanocomposites cover a wide range of uses, including energy storage, biomedicine, and photocatalysis, and are not solely concentrated on gas sensing.[1] Because

Monu Gupta

Mrs. Monu Gupta has received her MSc Physics degree in 1998 from R.D.V.V. University, Jabalpur, M.P., India. Currently, she is pursuing PhD Degree from Nanomaterials and Sensors Research Laboratory under the supervision of Prof. B. C. Yadav from the Department of Physics, Babasaheb Bhimrao Ambedkar University, U.P., India. Her area of research interest includes the preparation and properties of MXenes integrated with metal/metal-oxide/metal sulfide, especially for the gas-sensing applications relevant to the disease biomarkers.

Arpit Verma

Mr. Arpit Verma received his MSc degree in Applied Physics from Babasaheb Bhimrao Ambedkar University Lucknow, UP, India in 2018. Currently, he is pursuing a PhD degree from the Nanomaterials and Sensors Research Laboratory under the supervision of Prof. B. C. Yadav from the same university. His research interest includes the preparation and properties of metallopolymer-based functional nanomaterials for renewable energy applications, especially photovoltaics, photodetectors, sensors and energy-storing devices.

© 2023 The Author(s). Published by the Royal Society of Chemistry

Open Access Article. Published on 25 agosto 2023. Downloaded on 8/8/2025 16:09:06.
This article is licensed under a Creative Commons Attribution 3.0 Unported Licence.

of their exceptional physical, optical, electrical, and electronic properties, as well as their vast electroactive surfaces, MXene is a rapidly increasing family of novel materials in the post-graphene period.[2] The recently discovered carbides and nitrides have gained popularity and significant interest for gas sensing applications because of their outstanding chemistry and physical properties.[3] MXene features enormous surface areas, high surface-to-volume ratio, and different electronic structures with atomically thin layers due to their chemical and physical structure, which cannot be obtained with normal bulk structures.[4] The development of high-performance gas-sensing materials has drawn a lot of attention recently in comparison to conventional metal oxide-based gas sensors (MOS). A thorough review of the work on nanostructured gas sensors for VOC detection was previously presented by Mirzaei *et al.*[5] They addressed other VOC gas sensors in their review paper, although acetone received less focus. A review paper on room-temperature chemiresistive gas sensors by Joshi *et al.*[6] solely concentrated on room-temperature gas sensors, and covered other types of gases besides acetone. A solid and complete review on acetone gas sensors, which reviewed nearly all forms of gas sensors, was published by Alizadeh *et al.*[7] However, the review did not address metal oxide gas sensors specifically, and did not include a study that Masikini *et al.*[8] just released on the use of metal oxides to identify acetone in breath. Due to their numerous active sites, metallic conductivity, varied surface chemistry, and outstanding durability, MXene is preferred for gas sensing applications.[9] Given the substantial amount of research performed on them, MXene-based sensors may be one of the likely future materials for gas sensing in this context. The focused characteristics of MXene, such as their high flexibility, facile solution processability, and ease of functionalization, make it possible to combine them with other nanomaterials to create composites, opening up a new field of study for enhanced sensing performances.[10]

Toxins abound in the environment, endangering both humans and the environment. Every year, around 3.8 million people are killed by a variety of fatal illnesses caused by air pollution.[11] Additionally, according to the World Health Organization (WHO), these air pollutants harm the human nervous, immune, and respiratory systems, making people more vulnerable to risky diseases such as coronavirus disease (COVID-19), lung cancer, Chronic Obstructive Pulmonary Disease (COPD), ischemic heart disease, and stroke. Gas/vapor sensor devices are still used today to determine the concentrations of poisonous and non-toxic gases and to compute their amounts.[12] As industry and daily activities increase, along with the burning of fossil fuels, harmful gases and volatile organic compounds (VOCs) are emitted into the environment.[13] These VOCs and hazardous gases are poisonous to living things, including people and pets, when inhaled. Furthermore, the threats to our biosphere and other living beings are a concern. Among the several VOCs, acetone vapor is hazardous and possesses major human health problems.[14] At 300–500 parts per million (ppm), the potential effects of acetone vaporing in adults are nausea and irritation to body parts.[15] When a person has diabetes, either their body cannot produce enough insulin or they cannot

Priyanka Chaudhary

Ms. Priyanka Chaudhary is pursuing a PhD degree from BBA (Central) University, Lucknow. She received her BSc and MSc, MPhil (Gold Medalist) degrees in 2012, 2014 and 2016, respectively, from University of Lucknow, Lucknow and BBA (Central) University, Lucknow, U.P., India. She was selected for a six-month internship in the Taiwan Experience Education Program (TEEP) 2020 sponsored by the Ministry of Education Taiwan. Her research interest includes investigations on nanometallopolymers, quantum dots and 2D materials, and their applications in humidity and gas sensing.

B. C. Yadav

Prof. (Dr) B. C. Yadav was born in Hardatt Nagar Girant, Shravasti, Uttar Pradesh, India. Prof. Yadav received his PhD degree in 2001 from the Department of Physics, University of Lucknow, India. Currently, he is a Professor and the Head of the Department of Physics, School of Physical & Decision Sciences at Babasaheb Bhimrao Ambedkar University, Lucknow. Dr Yadav is also working as the Director of the University Sophisticated Instrumentation Center (USIC). He was the recipient of the prestigious Young Scientist Award (2005) instituted by the State Council of Science and Technology. Dr Yadav was also selected in 2011 for the Brain Pool International Fellowship of South Korea. He has published more than three hundred research/review papers in reputed international journals and authored two books. Dr Yadav has guided 24 PhD, 3 MPhil and 13 MTech students. Dr Yadav was nominated as a member of the National Academy of Sciences, India. His current research interests include the synthesis and characterization of metal oxide nanoparticles, metallopolymers, and Mxene with their applications as physical, chemical and biosensors.

 © 2023 The Author(s). Published by the Royal Society of Chemistry

Open Access Article. Published on 25 agosto 2023. Downloaded on 8/8/2025 16:09:06.
This article is licensed under a Creative Commons Attribution 3.0 Unported Licence.

use it efficiently. Typically, insulin works to metabolize blood glucose so that it may enter cells and produce energy. If the body is unable to obtain enough energy from glucose, it begins to burn fat as fuel.[16] Ketones are byproducts that are produced when fat is broken down for energy. Actually, acetone is a kind of ketone that the body produces as it breaks down fat for energy. Diabetics' bodies may produce a high level of ketones, resulting in diabetic ketoacidosis (DKA). DKA is a critical diabetes complication that can be dangerous for diabetic people. The presence of acetone in the breath implies that the body is producing a sufficient number of ketones, the acetone levels in a diabetic's breath can be used to determine their risk of DKA. A high quantity of acetone in the breath indicates that the body is creating a large quantity of ketones. So, acetone levels in the breath should be checked on a regular basis, and maintained within a diabetic's safe zone by medical therapy.[17] Diabetes mellitus is currently one of the top causes of death, with 0.451 billion diabetics globally in 2017 and a predicted increase to 0.693 billion by 2045. There are 200 different substances that have been identified in human breath, including the biomarker for diabetes known as acetone.[18,19] VOC and acetone sensors are gaining prominence because of their potential applications in health monitoring and self-monitoring. Because acetone is a specific biomarker for diabetes, its presence in human breath has been identified as an important indicator of the disease.[20] The average amount of acetone in the breath of healthy people is less than 1 ppm (0.3–0.9 ppm), but it increases to 2.2 and 1.7 ppm in type 1 and type 2 diabetic patients, respectively. As a result, recognizing acetone concentrations at less than 1 ppm, even at ppb levels, is crucial for detecting diabetes early.[21,22] Thus, the early detection of acetone is crucial in a range of disciplines, including indoor air quality monitoring, medical diagnostics, and the industrial sector, to reduce health risks.[23] As a result, it has become increasingly crucial in recent years to create high-performance gas monitoring sensors that can recognize minuscule amounts of acetone. Standardized techniques including high-performance liquid chromatography, proton transfer reaction mass spectrometry, and gas chromatography–mass spectrometry (GC-MS) can be used to determine the concentration of VOCs. These instruments cannot be used in portable healthcare applications since they are complex, challenging to use, and need time-consuming procedures to analyze the target gases.[24]

Due to their ease of fabrication, low cost, and high responsiveness, chemiresistive gas sensing materials have been used for a few years in the detection of several hazardous VOCs. Operation at high temperatures uses more energy, reduces the stability and longevity of the sensor, and puts the environment at risk of fire.[25] The primary responsibility of every sensor is to provide information about a variable that is essential to the operation. Every measuring device needs at least one sensing element. Another element found in the majority of measurement technique is the transducer.[26] The various types of gas sensors include chemiresistive, electrochemical, and infrared ones. With their superior accuracy, ease of use, and relative inexpensiveness, the chemiresistive sensors have received more attention than the other types.[27] The chemiresistive gas sensor detects gas by adjusting the sensor's electrical resistance, which is dependent on the sensing materials and the target gas, *via* a chemical process that occurs when the target gases come into direct contact with the sensing element.[28,29] This explains why chemical sensors have so many applications, especially in the medical field, where they are employed in portable healthcare monitoring systems.[30]

One of the most pressing issues in the realm of gas detection is the development of high-performance sensing materials at room temperature (RT).[31] Traditional techniques for detecting various VOCs have good sensitivity and accuracy. However, these techniques require large, intricate, costly, and time-consuming equipment, and necessitate the use of professional gas monitoring tools. As a result, small, transportable, and fast dynamic acetone detection instruments are needed.[32] When the target gases are present, electrical gas sensors can create an electrical signal. A useful gas sensor must have high sensitivity, selectivity, speed, stability, and affordability, as well as low cost and little power usage.[33] Gas sensors should also have a high signal-to-noise ratio (S/N), which evaluates the relative strength of the gas signal over the noise intensity. It is possible to assess the electrical noise of gas sensors by keeping an eye on the average resistance fluctuation before injecting the target gas.[34] A high electrical conductivity can typically create a low noise level. For calculating the limit of detection (LOD), at least three parameters among the five described above are required. N stands for the root mean square noise, and S is defined as average signal.[35]

In this review, we concentrated on the most recent developments in the study of bare MXene and its integrated nanocomposites for the detection of volatile organic compounds (VOCs). A road plan for commercializing MXene-based sensors is provided in this critical study, along with a thorough summary of current developments in sensor technology. Chemical, biological, and physical sensors are the three main classifications of the current sensors exhibited in Fig. 1.[36] Depending on whether a sensor uses an electrical, electrochemical, structural, or optical detecting mechanism, the four main ways that sensors function in each category are then divided into a variety of subcategories.[37] The most effective structural and electrical tactics for enhancing the performance of each category are provided. Finally, problems that prevent the commercialization of MXene-based sensors are examined, and many innovations for making MXene-based sensors readily available on a commercial scale are proposed. The production, properties, and uses of MXene in gas sensing devices are covered in this paper, along with information on their structural characteristics.

2. Classification of 2D materials

Owing to their morphology, high surface-to-volume ratio, and structural properties, 2D materials are applicable for gas sensing[39] because of their tunable chemistry, larger specific surface area, and fabrication techniques, 2D sensing nanomaterials have also been extensively studied in terms of the three S

Open Access Article. Published on 25 agosto 2023. Downloaded on 8/8/2025 16:09:06.
This article is licensed under a Creative Commons Attribution 3.0 Unported Licence.

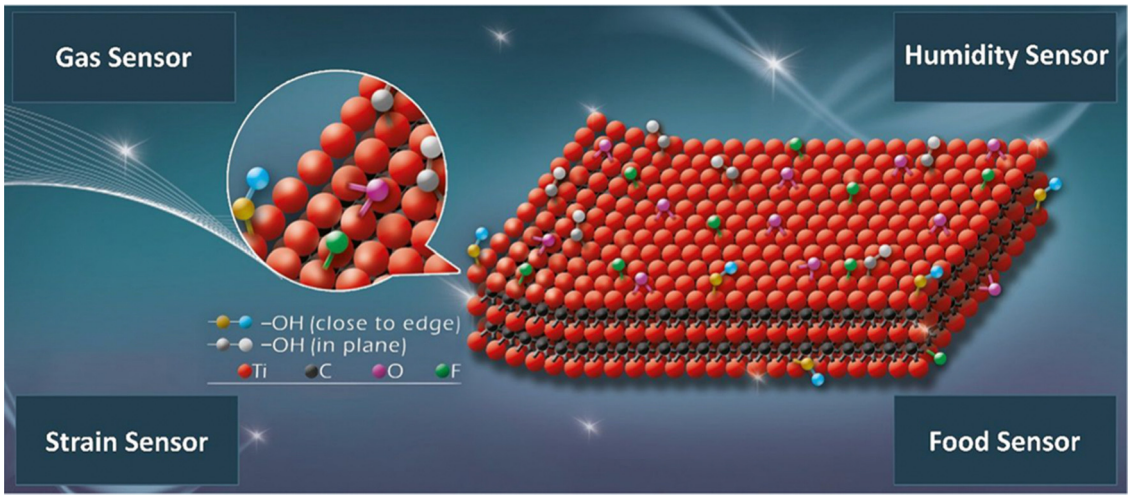

Fig. 1 Schematic diagram of MXene. Reprinted with permission from ref. 38. Copyright 2022, American Chemical Society Omega.

parameters (selectivity, sensitivity, and stability) and five essential R parameters (room temperature operation, repeatability, reproducibility, range of detection, response and recovery time).[40] Single-layer 2D materials with minimal or no interlayers have highly fascinating electrical properties that distinguish them from monolayers.[41] Fig. 2 shows many kinds of 2D materials, such as graphene, including Xenes, Xanes, Fluro-Xenes, Transition Metal Dichalcogenides (TMDCs), Sheet Moulding Compounds (SMCs), MXenes, and other 2D materials. These 2D materials are moderately fascinating to researchers owing to their physical and chemical properties, which vary from those of 2D bulk materials.[42,43] In these 2D materials, free charges do not move in one dimension, but move in the other spatial dimension. This feature of the 2D materials made it exceptional from other available bulk materials.[44] Additionally, 2D materials have a wide variety of elemental compositions that improve their insulating, semiconducting, spanning metallic characteristics, and fine-tuning can improve their electrical properties, which are good for gas sensing.[45] Ultra-thin 2D layered materials are famous for their unique chemical, physical, and electrical properties. This is why these materials are acceptable for energy storage, electronic application, and catalysis.[46] For room temperature gas sensing, the use of 2D materials is promising owing to their morphology and electrical properties.[45] These materials could be used in photocatalysts, field effect transistors, photovoltaics, composite materials, biosensors, photosensors and other applications.[47] Due to

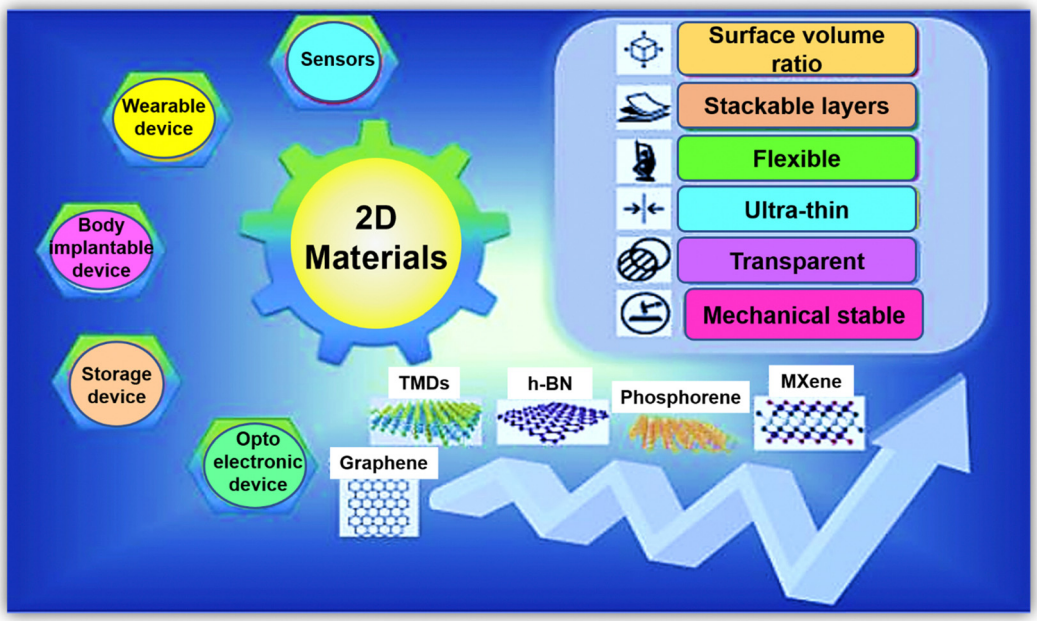

Fig. 2 A schematic illustration of 2D nanomaterials with their properties and application. Reprinted with permission from ref. 48. Copyright 2022 iScience.

 © 2023 The Author(s). Published by the Royal Society of Chemistry

Open Access Article. Published on 25 agosto 2023. Downloaded on 8/8/2025 16:09:06.
This article is licensed under a Creative Commons Attribution 3.0 Unported Licence.

their associated difficult synthesis processes, rough surface functionalization, and low selectivity, the 2D materials cannot be employed to produce sensing signals at the commercial level.

3. MXene: structures and properties

MXene has been accepted as a highly developed biosensing podium due to its excellent metallic conductivity, good biocompatibility, large surface volume ratio, and ease of functionalization.[49] It has already achieved much attention in the research field of electronics, sensors, catalysis, and energy.[50] MXene use in the biomedical sector has become a popular subject of research in the last two years, with studies on photothermal therapy for cancer, biosensors, neural electrodes, theragnostic, dialysis, and other applications.[51] In the field of biosensors, Xu and his coauthor began recommending 2D materials to study neural activity in 2015.[52] The MAX phase, as well as other layer nitrides and carbides, have been the focus of research for the last 10 years, and novel MXene precursors are now being developed since 2017.[53] The modern 2D material MXene is increasingly gaining acceptance in the realm of gas sensors. MXene, a brand-new material from the 2D family, was created in 2011 at Drexel University.[54] Shown in Fig. 3, as the forerunner of MXene, the MAX phase is frequently a sequence of triplex layered compounds, with M as the transition metal (Ti, Cr, Sc, V, Nb, Ta, Hf, Mo, and W), and A as an element such as Al or Ga, from group IIIA or IVA in the periodic table. This MAX phase is utilized as a precursor for the preparation of MXene.[55] MXenes are two-dimensional metal carbide, nitride, or carbonitride materials with layered hexagonal lattice formations with *P*63/*mmc* symmetry and the formula $M_{n+1}X_nT_x$.[56] Here, M is a transition metal (13 and 14 group element from the periodic table), *X* is a carbide, nitride, or carbonitride, and T_x is a terminated functional group, such as –O, –F, –OH.[57] By using the appropriate acid solution, such as HF, to etch the interlayer A atoms, MXene can be produced from the metal-ceramic MAX phase ($M_{n+1}AX_n$). In the MAX phase, M–A may be a covalent, ionic, or metallic bond and M–X may be a pure metallic bond.[58] Hence, at high-temperature, the M–A bond breaks down into $M_{n+1}X_n$, which brings about recrystallization and arrangement of 2D layered $M_{n+1}X_n$, and the MXene sheet is maintained with van der Waals force and hydrogen bond.[59] Recent studies have revealed a rapid increase in the variety of MXene compositions that have been synthesized.[60] To date, over 30 MXene compounds have been published, and over a dozen have been surveyed by using computational methods.[61] When two transition metals are mixed in the MXene structure, this is a characteristic property that is displayed.[62] Transition metals can be arranged in an ordered structure in a single exfoliated 2D MXene, either by creating atomic sandwiches of transition metals in the plane ($n = 1$) arrangement structure like $(Mo_{2/3}Y_{1/3})_2CT_x$ or for planes ($n > 2$) like $Mo_2TiC_2T_x$. MXenes were synthesized in 2014 and published in 2015.[63] The research on the MAX phase is exciting due to the numerous synthesized unique structured 2D carbide phases. The properties of the novel ordered double transition metal MAX phases have been studied, along with their magnetic properties. MXenes have an exclusive combination of properties. Along with the mechanical properties and electrical properties of the transition metal nitride/carbide, the functionalization surface of MXene makes it hydrophilic and prepared to attach with various species. This facilitates the creation of a durable colloidal solution in water with extra negative zeta potential and proper adsorption of electromagnetic waves. This is why there are a large number of MXene applications.[64]

The appeal of MXene stems primarily from the fact that, in contrast to other 2D materials (like graphene, transition metal

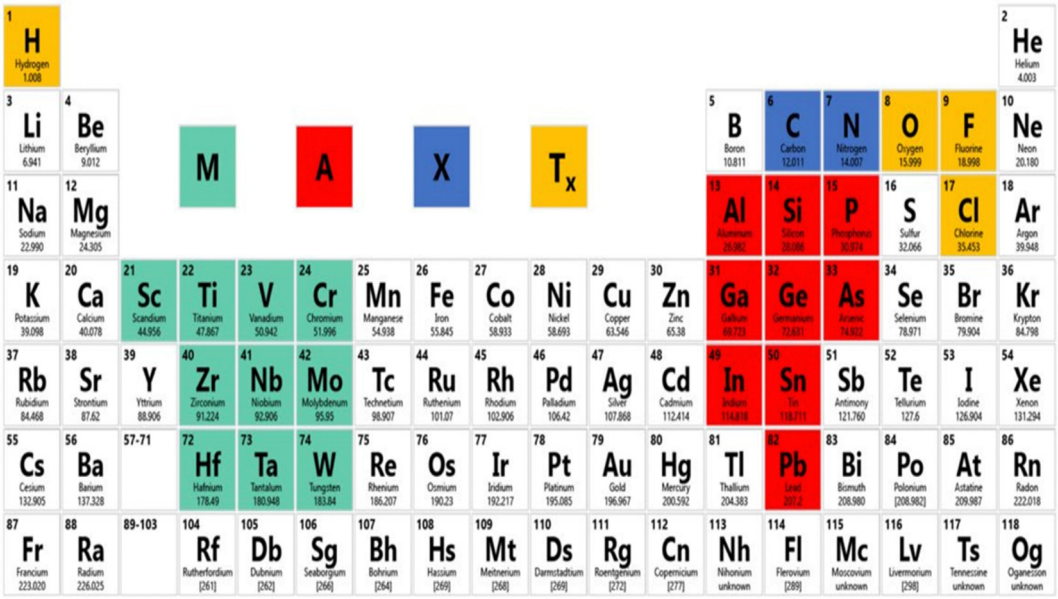

Fig. 3 Chemical elements for the design of the MAX phase and MXene. Adopted with permission from ref. 69. Copyright 2017, American Chemical Society.

Open Access Article. Published on 25 agosto 2023. Downloaded on 8/8/2025 16:09:06.
This article is licensed under a Creative Commons Attribution 3.0 Unported Licence.

disulfide, and hexagonal boron nitride sheets) that require difficult synthesis procedures, folding or re-stacking sheets, and have limited hydrophilicity, MXene is advanced in all features.[65] When a target gas comes into contact with 2D materials, the surface adsorption process can also affect the conductivity of the material.[66] However, with MXene, this is not always the case because the interlayer puffiness can drastically alter the surface properties. As a result, mechanisms other than adsorption may be required for gas detection. MXenes have adaptable surface chemistry, graphene-like morphology, redox capability with high conductivity, terminated function development on the surface, and overall outstanding hydrophilicity, which make them an ideal candidate for various sensor devices.[67] MXenes are now regarded as versatile gas-sensing materials, and it was noted that low concentrations of acetone can be detected at room temperature by utilizing an MXene-based sensing element.[68] The largely undiscovered members of MXene, which have a unique mixture of properties, open the door to a diverse array of applications.

3.1 Structure of MXene

The structure of MXene is similar to that of the MAX phase. However, the M atoms are tightly packed in a group, while the X atoms are located in octahedral interstitial positions.[70] In the hexagonal closed packed (HCP) configuration of the MXene structure, M atoms are arranged in M_2X in the same manner as they are arranged in M_3C_2 and M_4C_2 in an ABABAB and ABCABC sequence, respectively.[58] The MAX phase has a layered structure of carbides and nitrides with the formula $M_{n+1}AX_n$, where M is a transition metal (groups 3–7 in the periodic table), A is an element such as Al or Ga, from group IIIA or IVA in the periodic table, and X is either carbon or nitrogen. MXene is created when the A layer is eliminated by any etching method.[71] With the unstable M–A bond broken in the MAX phase, as shown in Fig. 4b, the elemental layers can be specifically eliminated, resulting in MXene with the formula $M_{n+1}X_nT_x$ (n = 1, 2, 3) and T_x as a surface termination functionality. The most significant change in the MXene structure occurs when the –O, –F, and –OH functional groups replace the transition

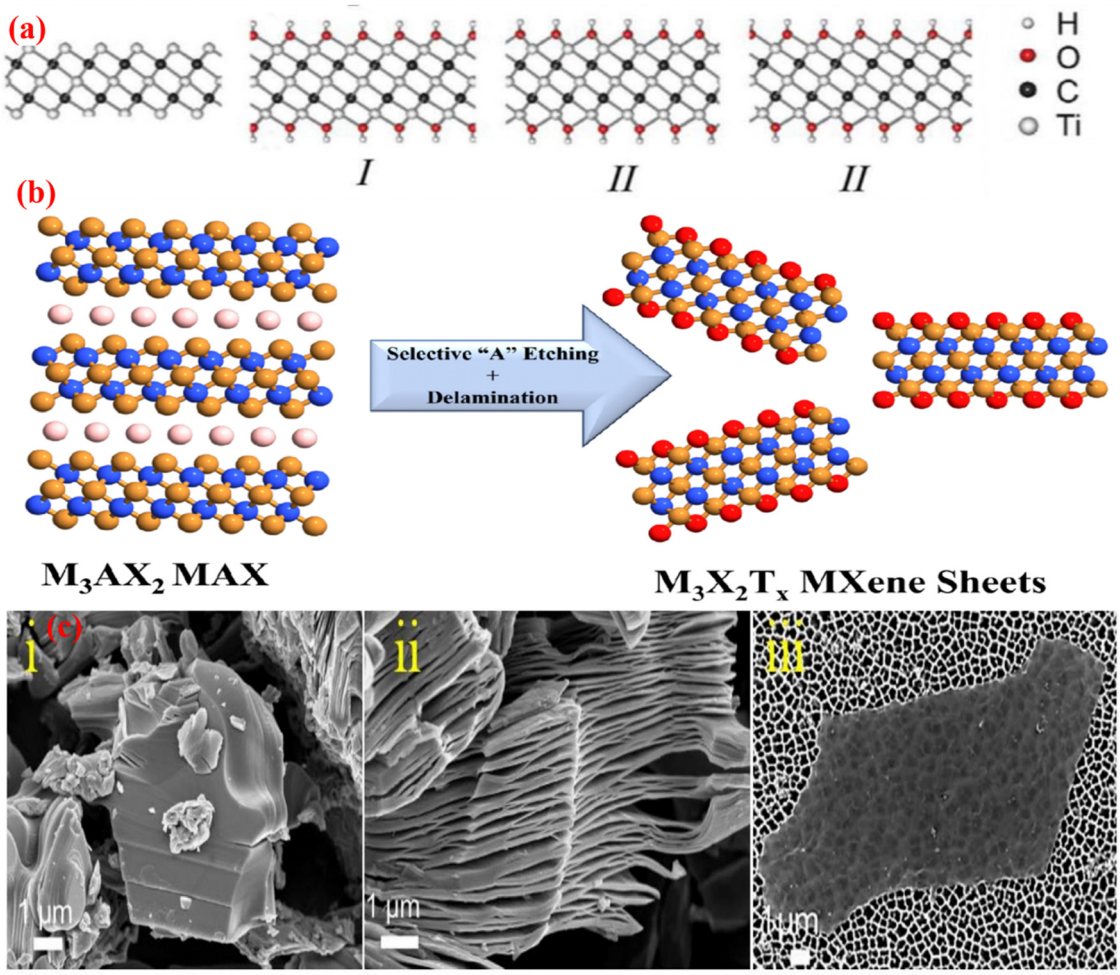

Fig. 4 (a) Configuration of the OH groups: (i) $Ti_3C_2(OH)_2$, (ii) $Ti_2C(OH)_2$, (iii) $Ti_3C_2(OH)_2$. Adopted with permission from ref. 73. Copyright 2012, Computational and Theoretical Chemistry, Elsevier. (b) Schematic illustration of the MXene synthesis process from the MAX phase.[74] (c) SEM images of the (i) MAX phase, (ii) Multilayer MXene, and (iii) MXene assembled flakes in a colloidal solution. Adopted with permission from ref. 62. Copyright 2017, American Chemical Society.

 © 2023 The Author(s). Published by the Royal Society of Chemistry

Open Access Article. Published on 25 agosto 2023. Downloaded on 8/8/2025 16:09:06.
This article is licensed under a Creative Commons Attribution 3.0 Unported Licence.

metal surfaces in the M–X layers as a result of the removal of the A layer from the MAX phase using fluoride acid, as illustrated in Fig. 4b and 4c (i and ii). Additionally, these functional groups, which are indicated by the symbol T_x in the MXene formula $M_{n+1}X_nT_x$, acquired some inherent flaws, such as atomic vacancies, during the preparation of the MXene flakes.[72] A. N. Enyashin *et al.*[73] used DFT (density functional theory) to determine the relationship between the properties and structure of MXene. In $Ti_3C_2T_x$, there are three different ways that –OH groups can be arranged. In configuration I, –OH groups are placed above the hollow space between the C atoms; in configuration II, –OH groups are positioned above the C atoms on both sides of layers; and in configuration III, they are mixed together. The structural stability of the term –OH configuration was assessed by contrasting their respective DFT energies. Configuration I is the most stable, whereas configuration II is the least stable because of the underlying C layers and strong attraction between T_x groups.[73] As a result, it was discovered that configuration I contains the functional groups –OH and –F. Different terminal groups provide MXene with a wide range of characteristics.

3.2. Properties of MXene

3.2.1 Tunable band gap. The shape and surface termination of MXene, which have a significant impact on sensory functions, may be efficiently controlled by the synthesis process. Micro/nano morphology, for instance, may be used to modify electrical characteristics when mechanical force is applied. Furthermore, multilayer morphology can aid the transport of enzymes for biosensors and allow for quick diffusion of certain compounds.[75] A handful of the newly discovered semiconducting MXene structures have band gaps greater than 1 eV, making them potentially useful for the production, delivery, and storage of renewable energy.[76] By examining the orbital decomposed electronic structures and density of states (DOS), we can provide information on the characteristics of semiconductors, such as Mott or charge-transfer insulators, as well as the primary excitation mechanism.[77] The core layer exhibits the leading N-2p to Ti-3d excitation, and the band margins of the surface layer exhibit a strong dominance of the M-3d states.[78] Layer-dependent and inter-atomic band edge-produced excitations in the two selected semiconducting MXene, which are accordingly charge–transfer semiconductors, permit careful research for novel optical properties.[79] The d states of Hf are the major source of the Hf_2CO_2 conduction band. This suggests that the band gap may be tuned by substituting Ti for Hf since Ti has lower d levels. The quasiparticle band gap of the semiconductor alloy $Hf_{2-2x}Ti_{2x}CO_2$ can be continuously adjusted from 2.45 to 1.15 eV, which is in line with the estimated quasiparticle band gap of Ti_2CO_2 of around 1.15 eV.[80] It is anticipated that adding Zr to the alloy system will lessen the lattice strain while essentially maintaining the same basic gap. MXene synthesis and modification are quite interesting, particularly in the context of sensors.

3.2.2 Physical properties. The physical properties of MXene are strongly influenced by their surface terminations. The elastic stiffness of MXene with –F and –OH terminations is lower than that of O-terminated MXene, even though MXenes with an O-termination are anticipated to have exceptionally high stiffness.[81] Here, the –O and –OH groups make MXene more stable because the –F group is replaced with the –OH group. When MXene is stored in water, –OH groups can also be replaced with –O groups by high-temperature treatment or metal adsorption method.[82] Most importantly, when MXene comes into contact with Al, Mg, Ca, or other metals, it can stimulate the breakdown of the –O groups into true MXene. The highest Young's modulus of MXene for a solution-processed 2D system is 330 GPa. Theoretically, MXene with lighter M elements and fewer layers (n = 1) is projected to have greater elastic moduli.[82] MXenes have a significant deal of potential for usage in composite materials due to their excellent elastic characteristics, as well as their strong electrical conductivity and hydrophilicity. Due to its suitability for intercalating a variety of organic molecules and metal cations,

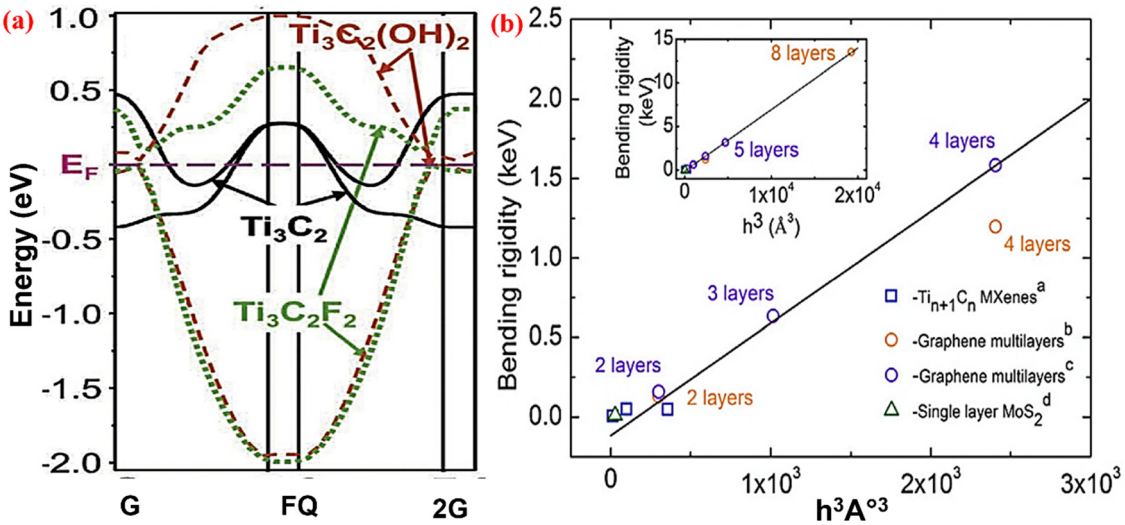

Fig. 5 (a) Electronic structure of the Ti_3C_2 MXene with OH, F functional groups, and no termination adopted with permission from ref. 96. Copyright 2011 John Wiley and Sons. (b) The bending rigidity of the $Ti_{n+1}C_n$ MXene, MoS_2, and graphene multilayer in relation to their thickness. Reprinted with permission from ref. 83. Copyright 2018 Elsevier.

Open Access Article. Published on 25 agosto 2023. Downloaded on 8/8/2025 16:09:06. This article is licensed under a Creative Commons Attribution 3.0 Unported Licence.

MXenes can be used in energy-storage applications. From Fig. 5b, we can observe the bending rigidity of the $Ti_{n+1}C_n$, MoS_2, and graphene multilayer as a result of their thickness. Thick MXene nanoribbons have a greater bending rigidity value. This is because it depends on different parameters, like the shape, size and temperature of the sample.[83]

3.2.3 Chemical properties. Many applications require the ability to produce exceptionally robust colloidal suspensions, particularly when fabricating thin films. The interlayer force is extremely strong in the bulk MAX phase, but it weakens after exfoliation in MXene. The formation of monolayers or few layers of MXene nanosheets is aided by the weak hydrogen bonding force between the –O/–F atoms on one surface and the –OH functional groups on the opposite surface, as well as the van der Waals force connecting the MXene layers.[84] This means that the surface termination configurations are highly dependent on the etching and exfoliation process with ambient temperatures, such as when Ti_3AlC_2 is etched with a low concentration of HF solution, to obtain $Ti_3C_2T_x$ and the amount of –O group will be greater than that of the –F group. In contrast, when Ti_3AlC_2 is etched with HCl–LiF solution for exfoliation, it contains the –O/–OH group with water molecules.[85] Consequently, the intercalation of water molecules and cations improves the $Ti_3C_2T_x$ dispersion behavior in various solvents. Furthermore, during the intercalation process and when cations and water molecules are introduced between the layers, they act as spacers.[10] Studies were performed to determine the most successful method for separating the forcefully bonded structure of MXene when intercalated with molecules, such as DMSO, urea, and isopropyl amine.[86] After exfoliation, a strong hydrophilic characteristic developed due to the creation of the surface termination on the $Ti_3C_2T_x$ nanosheets. As a result, the $Ti_3C_2T_x$ MXene shows the maximum dispersion stability in aqueous solution.[87] Thus, $Ti_3C_2T_x$-based materials like composite materials still blend with polymers, free-standing paper by filtration, and thin film for deposition.[88]

3.2.4 Electrical properties. MXene features a single-layer structure, metal-like electrical conductivity, and electron and Fermi level densities that are very close. The electrical conductivity of $Ti_3C_2T_x$ MXene is higher in comparison to other MXenes reported in the literature.[89] The electrical conductivity of MXene is affected by its shape, surface characteristics, and nanoflake size. Previous studies have reported that the least defective $Ti_3C_2T_x$ nanosheet had an electric conductivity of 6.5×10^{-3} S cm^{-1} and the largest defect obtained by $Ti_3C_2T_x$ etching with HF had an electrical conductivity of 1000 S cm^{-1}.[90] The MXene structure ($M_{n+1}C_nT_x$) contains $n + 1$ layers of M that are extremely close to one another, with C or N occupying the octahedral space between them to demonstrate the arrangement of $[MX]_nM$.[91] A metallic behavior is observed in the MXene family, such as $Ti_{n+1}X_n$. However, when the value of n grows, the metallic characteristics weaken due to the creation of an additional Ti–X bond. Titanium has greater metallic characteristics than titanium carbides in terms of X because N atoms have one more electron than C atoms.[92] By distinction, functionalized MXene sheets are small band gap metals or semiconductors, calculated by the species and position of surface groups. By literature survey, different terminated MXenes such as Hf_2CO_2, Ti_2CO_2, Zr_2CO_2, and Sc_2CF_2 have band gaps of 1.8, 1.03 0.45, and 0.24 eV, respectively. Here, $Sc_2C(OH)_2$ has a small direct band gap because its electronic structure can be tuned.[93] Strain can alter the interatomic distance and corresponding positions of atoms in materials. Therefore, when the tensile strain increases, the associated band gaps steadily become narrower. At the correct tensile strain, the indirect band gaps will become direct band gaps. So, under an external electric field in Sc_2CO_2 MXene, the indirect band gap changes into a direct band gap.[94]

DFT calculations also show that the band gap of MXene can be changed by changing the surface termination, as shown in Fig. 5a. MXene in Ti_3C_2 exhibits metallic behavior, whereas $Ti_3C_2T_x$ has functional groups with –OH and –F and behaves as a semiconductor with band gaps of 0.05 eV and 0.1 eV, respectively. As a result of their band gaps, these materials can be used in applications ranging from field effect transistors to semiconductors. The band gap of MXene can be changed by changing the elemental composition of the M layers. Anasori *et al.*[95] worked on the metallic nature of MXene like $Ti_3C_2(OH)_2$. When the top two layers of Ti were replaced with Mo and produced $Mo_2TiC_2(OH)_2$, the semiconducting properties were changed with a new bandgap at 0.05 eV. The density of state and atomic ordering calculation of $Ti_3C_2(OH)_2$ and $Mo_2TiC_2(OH)_2$ displayed this transition, which was verified by the negative and positive magneto-resistance values of both MXenes at 10 K.

4. Synthesis methods for MXene and Integrated MXene composite

4.1 Etching method of MXene (HF etching, intercalation, dispersion)

There are a variety of ways to make MXene from the MAX phase, including fluoride in an acidic solution, chemical vapor deposition, hydrothermal synthesis, alkali etching, and many others, which are given in Table 1. The two main methods for creating MXene are the bottom-up technique, which frequently begins with tiny atoms or molecules after crystallization and may be combined into a 2D layered MXene, and another one is the top-down method, which transforms bulk MAX phase transitions into single-layered MXene nanosheets.[97] From 2011 to 2020, the

Table 1 Different etching processes of MXene are used by etchants

MXene	Precursors	Etchants	Time (h)	T (°C)	Yield (%)	Ref.
$CrTiC_2T_x$	Cr_2AlC_2	5 M LiF + 6 M HCl	42	55	80	63
$Ti_3C_2T_x$	Ti_3AlC_2	50% HF	2	RT	100	96
$Ta_3C_3T_x$	Ta_3AlC_2	50% HF	72	RT	90	98
$Hf_3C_2T_x$	$Hf_3[Al(Si)]_4C_6$	35% HF	60	RT	NA	102
$Ti_3C_2T_x$	Ti_3AlC_2	3 M LiF + 6 M HCl	45	40	100	103
Nb_2CT_x	Nb_2AlC	50% HF	90	RT	100	109
$Zr_3C_2T_x$	Zr_3AlC_2	50% HF	60	RT	NA	110
Mo_2CT_x	Mo_2Ga_2C	3 M LiF + 12 M HCl	398	35	NA	111
$W_{4/3}CT_x$	$(W_{2/3}Sc_{1/3})_2AlC$	4 g LiF + 12 M HCl	48	35	NA	112
$Ti_3C_2T_x$	Ti_3AlC_2	1 M NH_4HF_2	12	80	NA	113

 © 2023 The Author(s). Published by the Royal Society of Chemistry

Open Access Article. Published on 25 agosto 2023. Downloaded on 8/8/2025 16:09:06.
This article is licensed under a Creative Commons Attribution 3.0 Unported Licence.

most widely used technique for producing MXene was the hydrofluoric acid (HF) etching process. The hydrofluoric acid (HF) etching technique was first employed in the Ti_3AlC_2 MAX phase by Naguib *et al.* in 2011 to remove Al layers by simple displacement reaction, and create hydrogen gas (H_2) using Ti_3C_2 MXene.[98] Ti_3C_2 MXene is generated as a result of DI water and HF acid solution, with different functional groups like $Ti_3C_2T_x$ (T_x as a functional group like –OH, –F, or –O). This was further processed, centrifuged and filtered because the supernatant contained the isolated solid form. In the next process, the layered structured MXene was found by washing with DI water and maintaining a pH of ∼6. The hydrofluoric acid etching method is mostly used to synthesize MXene materials.[99] The MXene particles in Fig. 4c(ii) have an accordion-like shape that is clearly visible. The temperature, duration, and F ion density all have a big impact on how well the MXene layers develop during the etching process. However, harder acid etching may give larger surface defects and may reduce the quantity of MXene.[100] Fig. 6a displays the good layered shaped $Ti_3C_2T_x$ MXene, which was produced by high concentration hydrofluoric acid. Chemical reactions used in the formation of MXene by HF etching are represented by eqn (1)–(3)

$$M_{n+1}AlX_n + 3HF \rightarrow AlF_3 + M_{n+1}X_n + 1{:}5H_2 \quad (1)$$

$$M_{n+1}X_2 + 2H_2O \rightarrow M_{n+1}X_n(OH)_2 + H_2 \quad (2)$$

$$M_{n+1}X_2 + 2HF \rightarrow M_{n+1}X_2F_2 + H_2 \quad (3)$$

Lower concentrated HF does not produce a layered morphology, whereas etching with high concentrations of HF results in a suitable separated layered structure with low MXene crystallinity.[72] The etching procedure depends on many variables, including the type of etchant, etching duration, temperature, and MAX phase quality, MXenes $Ti_3C_2T_x$,[96] Nb_2CT_x,[101] $Hf_3C_2T_x$,[102] *etc.* MXene is produced using this process, resulting in enormous amounts of very poisonous HF fumes that are hazardous to health.

To ensure safety and halt the disastrous results of concentrated HF, an alternative method must be used. The MAX phase was immersed for 45 hours at 40 °C in a solution of lithium fluoride (LiF) and hydrochloric acid (HCl) to etch the aluminum

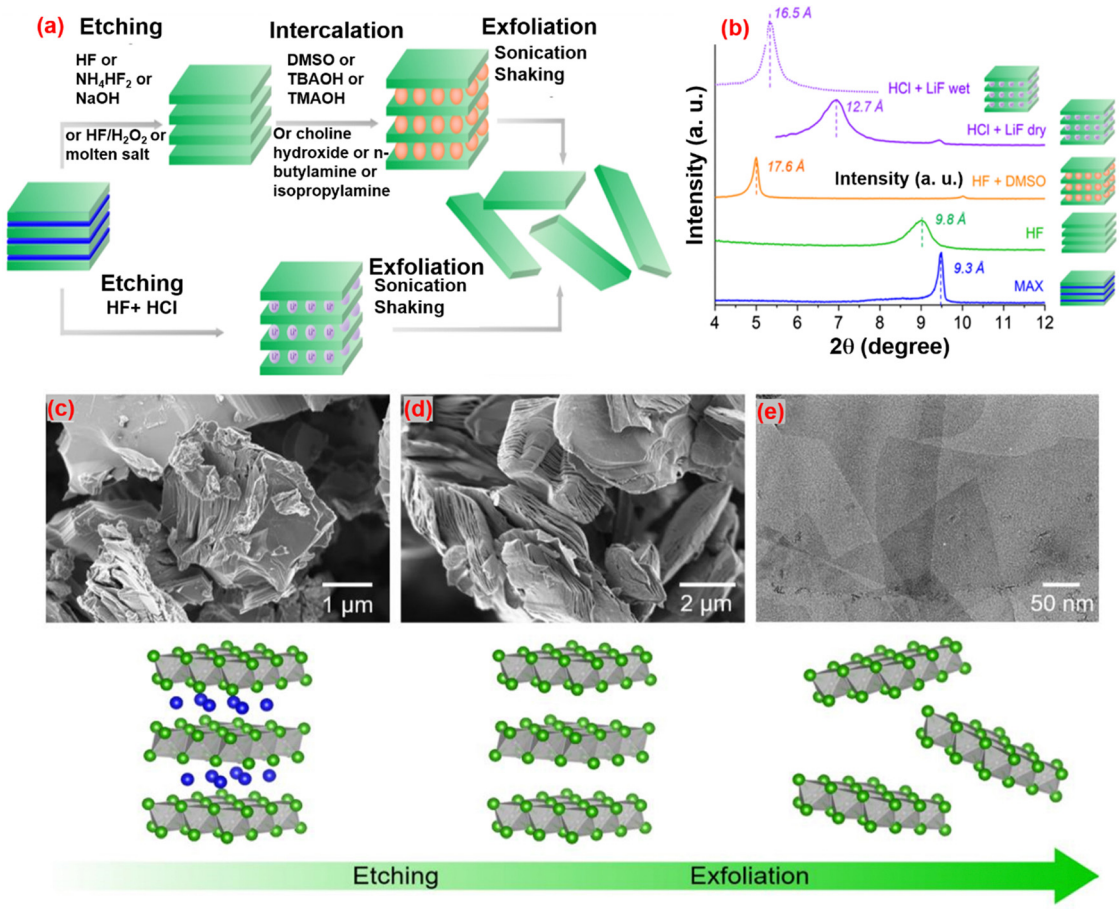

Fig. 6 (a) Pathway to obtain 2D MXene single flakes by top-down synthesis: first, selective etching of atomic layer(s) from a 3D layered precursor is required, followed by exfoliation into single flakes. (b) XRD patterns for Ti_3AlC_2 (blue), dry $Ti_3C_2T_z$ multilayers after etching with HF and washing (green) and after intercalation with DMSO (orange), dry (solid line purple) and wet (dotted line purple) $Ti_3C_2T_z$ multilayers etched with HCl+LiF. (c) SEM micrograph of Ti_3AlC_2 particles. (d) SEM micrograph of $Ti_3C_2T_z$ multilayers after etching of the Al layer. (e) TEM micrograph of overlapping $Ti_3C_2T_z$ single layers. Schematics of the MAX-to-multilayers MXene transformation and their exfoliation are shown in the bottom row.[71] Copyright 2019 Current Opinion in Solid State & Materials Science.

Open Access Article. Published on 25 agosto 2023. Downloaded on 8/8/2025 16:09:06.
This article is licensed under a Creative Commons Attribution 3.0 Unported Licence.

layers from the MAX phase. This process was introduced by Ghidiu *et al.*[103] due to the mild nature of LiF + HCl. However, some defects appeared, so other combinations of fluoride salts can be used, such as NaF, CsF, CaF_2, KF with HCl or H_2SO_4.

$$LiF_{(aq)} + HCl_{(aq)} \rightarrow HF_{(aq)} + LiCl_{(aq)} \quad (4)$$

This method is less harmful, produces fewer defects, and requires less sonication time. Most importantly, HF etching failed for the nitride-based MXene.[104] Using this method, many MXenes, such as V_2CT_x,[105] Mo_2CT_x,[106] and $W_{4/3}CT_x$,[107] have been prepared. Only NH_4HF_2 should be used for the MAX phase of the Ti_3AlC_2 etchant, rather than a strong acid. In addition, as the MXene layers were being etched, NH^{4+} (ammonium) ions were intercalated into them. This technique produced layers with a larger lattice parameter than HF etching in Ti_3C_2, which was the previous approach used. The etching process of Ti_3AlC_2 by NH_4HF_2 is explained through eqn (5).

$$Ti_3AlC_2 + 3NH_4HF_2 \rightarrow (NH_4)AlF_6 + 3/2H_2 + Ti_3C_2 \quad (5)$$

To achieve high MXene quality, the etching procedure and suitable conditions must be gradually changed. For weak etchants, such as LiF/HCl, NH_4HF, and NH_4F, a long etching time or a high reaction temperature are required. The MXene structure verifies the outcome, requiring additional time and a higher temperature. A larger *n* value requires a greater fluorine ion, as well as a high reaction time.[108]

Multilayered MXene must then undergo a delaminating process to generate single-layered MXene.[114] Reducing the contact between layers in MXene requires increasing the interlayer gap using intercalating materials.[115] A suitable solvent is necessary for the delamination and intercalation processes to scatter the material and intercalate the products effectively. When the intercalated-like organic molecules dissolve in the solvent and are agitated for a few hours, they can fit between the 2D layers of multilayered MXene, resulting in a swollen shape as the interlayer distance rises. Furthermore, sonication in deionized water can convert the intercalated MXene multilayer into mono sheets.[116] The sonication procedure is critical for the final nanosized sheets. Organic chemicals and ionic compounds are the two forms of intercalation. Organic chemicals are commonly employed as intercalants for HF-produced MXene because they mostly comprise polar organic molecules, such as isopropylamine, hydrazine, dimethyl sulfoxide (DMSO), urea, and tetrabutylammonium hydroxide (TBAOH).[58] For delaminating, $Ti_3C_2T_x$ and Nb_2CT_x have been used with DMSO and isopropylamine intercalants. Meanwhile, for the delamination of Mo_2CT_x, V_2CT_x, $Ti_4N_3T_x$, and Ti_3CNT_x, TBAOH was used as for intercalation.[58]

Due to a van der Waals force acting between the layers of MXene, MXene can be piled below its weight. It directs the increase of the ion transport pathway, and decreases the contact between electrolytic ions and active surface sites. This is why it is necessary to find a method that allows MXene to still be dispersed.[117] Usually, two techniques are used together, not only in modifying MXene, but also in choosing various dispersants. Regarding dispersants, the most researched solvents have been organic. Maleski *et al.*[118] dispersed the MXene in ethanol, acetone, water, methanol, and other solvents. The ease of dispersing the 2D substance with the solvent increases with surface tension. Except for ethanol, all other organic solvents have extremely high surface tension. For example, the solution-phase flocculation technique primarily used ammonium ions to resolve the MXene re-stacking issue. This technique was first used by Zhang *et al.*[119] for the preparation of $Ti_3C_2T_x$ MXene, although the direct preparation of MXene powder was possible using the solution-phase flocculation technique.

4.2 Synthesis of the integrated MXene composite

MXenes are regarded as ideal prospects for the synthesis of multifunctional composites due to their 2D morphology, multilayered structures, and remarkable flexibility, which has sparked a rise in the research of MXene-based composites. Many unique composites have been created by mixing MXenes with other materials, such as polymers, metal oxides, and carbon nanotubes.

4.2.1 Mxene–polymer composites. MXenes with superior mechanical characteristics, metallic conductivity and hydrophilic surfaces can improve the mechanical and thermal properties of polymers when building composites with polymers. Single-layer MXenes have easily accessible surface hydrophilicity and polymer compatibility compared to multi-layered MXenes. As a result, MXenes are often delaminated before interacting with polymers. Ling *et al.*[120] described the production of a single-layered $Ti_3C_2T_x$–polyvinyl alcohol (PVA) composite by combining a colloidal solution of $Ti_3C_2T_x$ films with an aqueous solution of PVA. The PVA was spread between $Ti_3C_2T_x$ films in the $Ti_3C_2T_x$–PVA composite, which is a layered structure. Naguib *et al.*[121] used a two-step approach to create a $Ti_3C_2T_x$–polyacrylamide (PAM) composite. First, DMSO was inserted into the $Ti_3C_2T_x$ interlayers to enhance the $Ti_3C_2T_x$ layer separation and obtain complete delamination of the individual $Ti_3C_2T_x$ layers. The produced $Ti_3C_2T_x$ and PAM solutions were then evenly mixed and dried for 4–5 days at room temperature.

4.2.2 MXene-metal/metal oxide composites. MXene-metal/metal oxide composites have excellent electrochemical stability and strong electrical conductivity. The synthesis of the Au/$Ti_3C_2T_x$ nanocomposite was accomplished by chemical reduction. In this procedure, a reducing agent was introduced to decrease the metal-containing solution, and stirring was also used to help. The previous combination was then added with $Ti_3C_2T_x$ MXene. After 30 minutes, the chemical was ultrasonically treated. After the reaction was finished, the solution was drained using cellulose filter paper with 0.1 μm pore size and rinsed three times with deionized water. After that, the filtered material was dried for two hours at 80 °C in a vacuum oven.[122] Wang *et al.*[123] offered a straightforward method for producing a $Li_4Ti_5O_{12}$–$Ti_3C_2T_x$ composite. The comparable synthetic process comprises two steps. To begin, by combining $Ti_3C_2T_x$, different hydrogen peroxides, and $LiOH{\cdot}H_2O$ in deionized (DI) water, lithium ions can enter the interlamination of $Ti_3C_2T_x$ and increase its interlayer spacing. The acquired products are then washed multiple times with DI water and dried at 40 °C for 24 hours before being calcined at 550 °C for

 © 2023 The Author(s). Published by the Royal Society of Chemistry

Open Access Article. Published on 25 agosto 2023. Downloaded on 8/8/2025 16:09:06.
This article is licensed under a Creative Commons Attribution 3.0 Unported Licence.

4 hours under N_2 atmosphere to achieve the final products. Zhu *et al.*[124] created TiO_2–$Ti_3C_2T_x$ nanocomposites in a hydrothermal environment. The TiO_2–$Ti_3C_2T_x$ nanocomposite is formed by heating the sample at 500 °C for 4 hours after tetra butyl titanate (TBOT) combines with $Ti_3C_2T_x$ to create precipitates of TiO_2 particles that attach to the surface of $Ti_3C_2T_x$.

4.2.3 MXene-carbon nanotube composite. These composites were created through mechanical mixing, co-dispersion, self-assembly, electrophoretic deposition, *in situ* CNT growth on MXene by chemical vapor deposition, thermal processing, hydrothermal methods, and microwave-assisted synthesis.[125] Three-dimensional (3D) nano-fillers of MXene ($Ti_3C_2T_x$)/CNTs have been synthesized with high stability and enhanced interfacial attachment between adjacent fiber yarns, as well as increased tensile and flexural strength, demonstrating excellent roughness on the surface and elasticity even after 18 weeks of immersion in alkali solutions.[126]

4.3 Characterizations of MXene and its integrated composite

4.3.1 X-ray diffraction analysis. The best technique to ensure that there are no interacting MAX phases is by using X-ray diffraction (XRD) after imparting considerable texture to the powders. Because MAX phases are extremely anisotropic, when pressure is applied to the powders, the particles arrange along the (002) direction. This points out (00l) peaks in all MAX phases, making it simpler to identify conflicting MAX phases. It should be noted that texturing the materials in this manner makes complete phase quantification by Rietveld refinement. As a result, it is preferable to run the scan twice, once untextured and then again textured.[127] In addition, the formation of the MXene composite increases the space between interlayers and specific surface area. Due to these remarkable properties, the adsorption and sensitivity performance are enhanced. MXene is identified by the XRD peak (110) at the 2θ value of 60° for the layered configuration form. In the etching process at the proper time, the peak (002) gets shifted at a lower angle. Fig. 6b and 7c exhibit the XRD pattern of the Mo_2Ga_2C MAX phase and Mo_2CT_x MXene after being HF etched. Hence, a strong peak (002) can be observed at a lower angle (<10°), and the XRD pattern also indicates the expanded interlayer spacing after etching with HF.

4.3.2 Raman spectroscopy. Vibrational spectroscopies are powerful techniques for identifying molecular patterns, and have been widely utilized to detect the structure of 2D materials. Raman- or infrared-active vibrations are determined by the space group of the material. Fig. 7d shows that material uniformity should be addressed when interpreting a vibrational spectrum. The structure of MXene is characterized as a deformed *P*63/*mmc* space group. Surface groups are responsible for the distortion. This causes the vibrational bands to enlarge,[128] because only one unit cell is included in simulations, the available estimations are based on the structure, which assumes homogeneous surface groups. In practice, the MXene synthesis method produces several surface groups that are randomly distributed around

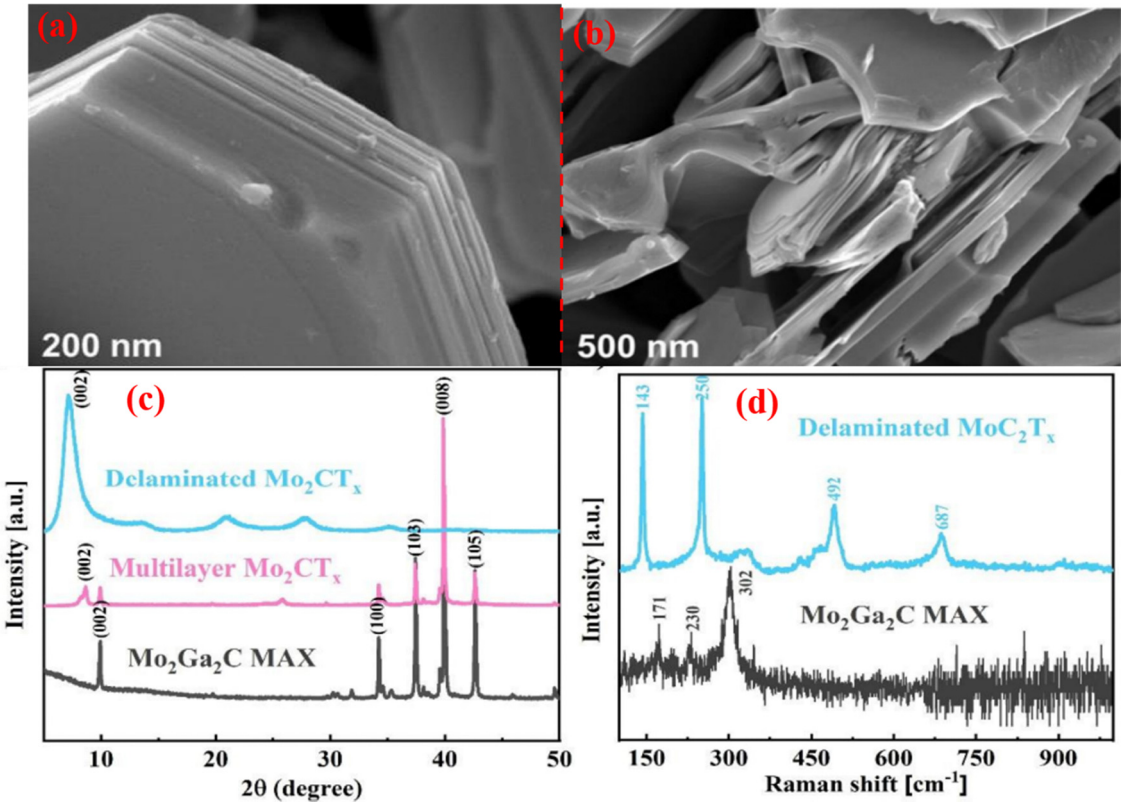

Fig. 7 SEM images of the (a) Mo_2Ga_2C Max phase, (b) after HF etched Mo_2CT_x MXene, (c) XRD pattern of Mo_2Ga_2C during HF etching, (d) Mo_2Ga_2C MAX phase and delaminated Mo_2CT_x MXene Raman spectra. Reprinted with permission from ref. 130. Copyright 2020 American Chemical Society.

Open Access Article. Published on 25 agosto 2023. Downloaded on 8/8/2025 16:09:06.
This article is licensed under a Creative Commons Attribution 3.0 Unported Licence.

the flake. This causes a superposition and overlap of the surface group vibrations, and peak widening, making Raman spectral interpretation extremely difficult. Furthermore, the presence of water between the layers has an effect on the IR spectrum. However, good sample preparation may decrease this impact and allow infrared spectroscopy to reach its full potential, particularly for composite materials. In place of FT-IR, Raman spectroscopy was employed to demonstrate the presence of MXene in the composite materials.[129]

4.3.3 Scanning electron microscopy. SEM enables identification of the structure, and typically provides immediate confirmation that MXene is being produced. However, not every single etched sample seems to be the same. Since the first MXenes were formed by immersion in extremely concentrated HF, the ''accordion'' form is thought to be indicative of a successful synthesis, as exhibited in Fig. 6c and d. Fig. 7a shows a pure layered stature of the Mo_2Ga_2C MAX phase and the multilayered structure of Mo_2CT_x MXene, which can be obtained after etching with HF. However, its accordion structure, which is now virtually synonymous with MXene, does not characterize all multilayer MXenes.[62] Fig. 7a and b show the difference between the MAX phase and the MXene morphology. Energy dispersive X-ray spectroscopy (EDS) is frequently used in conjunction with SEM as a supplementary method. While this method provides good qualitative information regarding the M element, it is critical to recognize that it is not accurate for analyzing the surface terminations or X ratios. Even when analyzing multiple-M MXenes, it is preferable to employ a qualitative comparison rather than an exact quantitative study. This is because most of the EDS detectors in use are not quantitative and calibrated as such. It is feasible to employ EDS as a quantitative approach.[131]

5. MXene-based acetone sensors: a mechanism

MXenes have high conductivity and typically exhibit metallic characteristics. The donor or acceptor gas molecules, as well as the p-type or n-type sensing materials, determine whether resistance increases or decreases in the semiconductor gas mechanism.[132] In 2D materials, the space between the layers is a crucial for electrical transport. Large gaps between the 2D MXene provide a fundamental pathway for the movement of electrons. Junkaew and others[133] have worked on the interlayer expansion that would change the conductivity of the materials and enhance the gas sensing performance. In 2D materials, the interlayer spacing is enhanced as a result of layer expansion, and electrons are unaffected. Additional active sites for gas adsorption may be added to MXene by the active terminations. In comparison to gas sensors based on other 2D materials, MXene-based gas sensors have extremely high signal-to-noise ratios and low limit of detection (LOD).[134] Furthermore, despite the MXene gas sensor's ability to detect both electron acceptor gas and electron donor gas, the change in MXene resistance constantly rises. Chen *et al.*[135] found that in the detection of acetone and ethanol, the resistance changes were typically positive. While the MXene carriers shrank and the MXene surface started to take up gas molecules. As the output increases, the MXene resistance increases. MXene can be characterized as having strong hydrophilicity and solution processability.[136] The primary reason that MXene constantly shows a positive resistance is that the barrier on the surface of MXene makes it harder for the electrons to move around. This causes MXene to have more resistance, whereas other 2D materials do not experience it.

Following the etching procedure, MXene absorbed H_2O and O molecules. This caused p-type MXene doping, which changed the metallic MXene behavior into that of a semiconductor. The MXene gas sensing mechanism is now understood similarly to semiconductor materials. The MXene sensor takes in oxygen when it is exposed to air. O_2 molecules may be adsorbed on semiconductors by gaining an electron,[137] and finally change them into chemically adsorbed oxygen molecules like O^{2-}, O_2^-, and O^-. After the surface produced the oxygen molecule O_2, layers of hole accumulation formed, lowering electron resistance. O_2 on the surface of sensor reacts with the target gas when the MXene sensor is submerged in it. Due to electron–hole recombination, which decreases the carriers of the MXene sensor and increases resistance, the electrons taken by the O_2 molecule are free to return to the MXene surface.[138] When metallic MXene and n-type semiconductors are mixed, the Fermi level remains constant, while electron transport occurs between the two materials and creates an electric field and Schottky barrier as a result. The MXene gas sensor's gas sensing mechanism is improved as a result of the interfacial generation of p-n junctions. As a result, the electron acceptor or donor property of the target gas molecule determines whether the sensor resistance negatively or positively changes. For instance, the p–n heterojunction of $SnO–SnO_2/Ti_3C_2T_x$ is shown in Fig. 8b and c. The energy level structure prior to contact and the acceptable band diagrams for SnO, SnO_2, $Ti_3C_2T_x$ MXene are shown. The band bending is caused by the differing Fermi levels after the combination (Fig. 8b), as the charge carrier changes until the Fermi energy is equal. Both p-type MXene and n-type semiconductor have a lower work function. The electron transfers from the n-type semiconductor and p-type MXene to the n-type semiconductor with oxygen adsorption/desorption occurring on the sensing material surface through exposure to sensing analyte. The oxygen is then removed by the target gas, and creates a depletion layer, as shown in Fig. 8c. Before exposure to air, the electron resistance of the n-type semiconductor/p-type MXene will increase.[139] As seen in Fig. 8d, when acetone gas is introduced, it oxidizes the oxygen that has been adsorbed. Electrons are then released and returned to the n-type semiconductor/p-type MXene sensing materials. The hole reacts with the liberated electron, raising the Schottky barrier height, which is the cause of the increased resistance. The n-type semiconductor/p-type MXene has a higher resistance than n-type semiconductors as a result of the electron depletion layer's thickness, which decreases. The following eqn (6) and (7) explain how the adsorbed oxygen and acetone undergo an oxidation–reduction reaction.

$$O_2 + e^- \rightarrow O_2^-(ads) \quad (6)$$

 © 2023 The Author(s). Published by the Royal Society of Chemistry

Open Access Article. Published on 25 agosto 2023. Downloaded on 8/8/2025 16:09:06.
This article is licensed under a Creative Commons Attribution 3.0 Unported Licence.

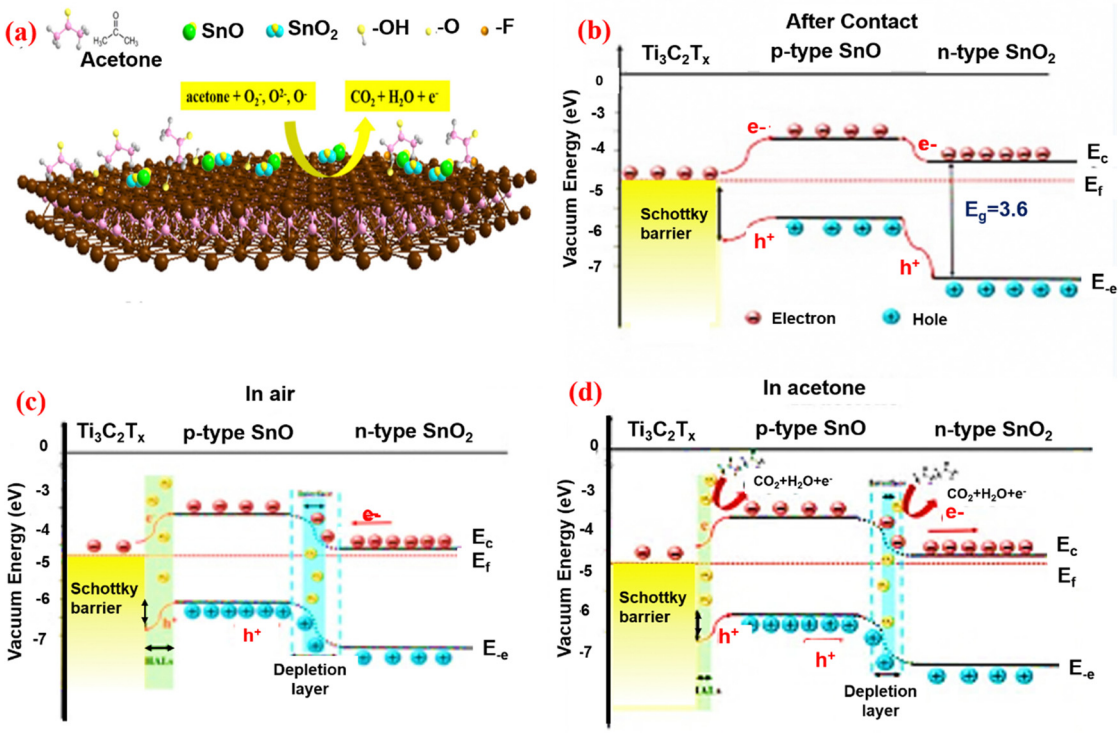

Fig. 8 Schematic illustration of the band diagram of the p–n heterojunction and the combination of the SnO–SnO_2/$Ti_3C_2T_x$ sensor. Adopted with permission from ref. 139. Copyright 2020 Material Science Technology.

$$CH_3COCH_3 + 4O_2^- \rightarrow 3CO_2 + 3H_2O + 4e^- \quad (7)$$

The n-type semiconductor/p-type MXene sensor will exhibit a hamburger-like morphology due to the wide surface area, which provides sufficient adsorption and reactivity for oxygen and the target gas. This is only one example of numerous contributions of MXene toward improving gas sensing performance. MXene has a significant amount of additional oxygen functional groups (–OH, –O) on its surface.[139] MXene is now viewed as a versatile gas sensor, and the first finding of low-concentration acetone at room temperature was detected.

5.1 VOCs sensing by MXene

Gas sensing is a growing research direction because of its utilization in air quality management for monitoring air pollution, diagnosis, and breath analysis.[140] Apart from reactive gases like NO_2, H_2S, and NH_3, the identification of VOCs at ppm/ppb concentrations is essential for the early prediction of serious disorders like peptic ulcers. Normally, high noise and signal bandwidth are the two important factors for generating sensitive gas sensors.[141,142] In this way, the sensing podium can accommodate numerous active sites and high conduction for interfacial interaction.[143] There is a trade-off relationship in traditional materials like metal oxide, graphene, and black phosphorus, which can be categorized as materials that are considered but not optimal for sensing applications.[144]

Due to their special qualities and possible benefits over conventional sensing materials, MXenes are crucial for the detection of volatile organic compounds (VOCs). Because MXenes have a wide surface area, there are many active sites for gas adsorption.[145] This quality makes MXene-based sensors more sensitive towards VOCs, and enables the detection of low quantities. MXenes can be tailored in terms of composition by using different transition metals and functional groups in the synthetic process.[146] The selectivity and sensor performance of MXenes can be improved for certain VOCs because of its tunable characteristics. Good electrical conductivity, which is essential for creating capacitive or resistive gas sensors, is exhibited by MXenes.[1] Changes in gas adsorption on MXene surfaces can result in changes in electrical characteristics, allowing for the conversion of quantifiable signals from the gas concentration. Even in the presence of VOCs and other reactive gases, MXenes remain chemically stable. MXene-based gas sensors reliably operate over an extended time because of their stability, which is beneficial for applications requiring continuous monitoring.[132] Real-time VOC identification is made possible by the demonstrated quick response times of MXenes. The huge surface area is responsible for their quick response time since it enables quick gas adsorption and desorption processes. Thin films, nanosheets, composites, and three-dimensional structures are just a few of the sensor configurations that may include MXenes. This adaptability enables the creation of several sensing systems specifically suited for various VOC sensing applications. When compared to other 2D materials like graphene, MXenes are comparatively inexpensive.[147] They are appealing for mass manufacture and extensive use as VOC sensors due to their cost-effectiveness. Owing to these attributes, MXenes are promising

Open Access Article. Published on 25 agosto 2023. Downloaded on 8/8/2025 16:09:06.
This article is licensed under a Creative Commons Attribution 3.0 Unported Licence.

materials for VOC sensing, opening the way to the creation of sensitive, focused, and dependable gas sensors for use in applications, such as environmental monitoring, workplace safety, and indoor air quality. The performance and usability of MXene-based gas sensors are being further explored and improved *via* ongoing research, which will help with VOC sensing.[134]

MXene is a potential candidate in sensing materials due to its unique properties of having a hydrophilic surface, metallic conductivity, and 2D layered structure. As a result, MXene has been included in the field of gas-sensing biosensors, piezoresistive sensors, optical sensors, and gas-adsorptive sensors.[163] In 2015, Xu and his collaborator started to recommend 2D materials in the biosensor field for exploring neural activities. They utilized a thin MXene micropattern to recognize highly sensitive FET biosensors for the label-free testing of small molecules in a proper biological environment and quick detection of action potential in initial neurons.[164] This work developed a new space for biosensing applications to utilize MXene, showing that MXene can be a favorable candidate for expanding biosensors due to their outstanding electrical properties, large surface-to-volume ratio, and excellent biocompatibility. The MXene biosensor shows outstanding stability, repeatability, and reproducibility. Even though further extensive research has been performed on MXene-based sensors, these excellent properties do not meet all of the requirements of different applications.[165] Hence, surface moderation and functionalization are compulsory to improve their performance. Meanwhile, a different potential problem is that physical adsorption interaction and noncovalent bonds are not durable in some biomedical applications. So, a possible interpretation could be to adopt the improved functional group on the surface of MXene-based materials to include some unique and controllable binding on the surface to enhance the surface properties.[166]

According to Table 2, the most recent research suggests that Ti_2C MXene works well as a sensor for NH_3 gas detection. Similar to whole cell application, lowering the applied biaxial strain makes it easy to release the NH_3 that has been absorbed on single-layered Ti_2CO_2. However, once NH_3 is omitted, Ti_2CO_2's electrical conductivity rises.[167] The most popular option for NH_3 sensors is the O-terminated MXene. When $Ti_3C_2T_x$ MXene electrodes are used, the confined biological receptors on the surface of the nanosheet act as transducers, resulting in efficient sensing performance. This enables a direct electron transfer (DET) between the electrode surface and the redox enzyme to occur. Enzymes and proteins can be freely immobilized on the surface of MXene.[168] As a result, they can be utilized to assist DET, lower detection thresholds, increase sensitivity and selectivity, and increase electrode kinetics. $Ti_3C_2T_x$ MXene has been used to electrochemically identify several biomolecular components.[169,170] Recently, a $Ti_3C_2T_x$/Nafion/AuNP nanohybrid created a glucose biosensor having a glassy carbon electrode coated with a material that can immobilize glucose oxidase (G_{ox}).[171] Due to the large specific surface area and unique organ-like structure of the hybrid Ti_3C_2/TiO_2, the limitation of the substrate was confirmed. Additionally, a successful collision between redox proteins and substrate would occur when enzymes mounted on the surface of Ti_3C_2/TiO_2 nanosheets were found. As a result, the sensing capabilities of biosensors were improved.[172]

To manage the health risk, acetone must first be identified by judgment in a variety of disciplines, including medical diagnosis, indoor air quality monitoring, and industrial area. Because of this, it is imperative to create high-quality monitoring sensors that are capable of detecting acetone at ppm or ppb levels. For diabetics, acetone is a crucial biomarker; thus, acetone sensors should be used to detect acetone concertation in human breath. Yongshan Xo *et al.* reported on a $W_{18}O_{49}$/α-Fe_2O_3 hollow structure for the detection of acetone. Its response/recovery time is 10/31 s and a detection limit of 86 ppb.[173] S. Sun *et al.*[156] reported on the $W_{18}O_{49}$/$Ti_3C_2T_x$ composite fabrication for acetone sensing. MXene is a suitable candidate for use in gas sensing and biosensors due to the availability of functional groups on its surface. These functional groups can efficiently generate active

Table 2 Summary of MXene-based VOC sensors

MXene	Method	Gas	Concentration (ppm)	Temp (°C)	Response/recovery time (s)	Ref.
Mo_2CT_x	HF	Toluene	140	RT	—	130
$Ti_3C_2T_x$	3.2 g + 9 M HCl	Ethanol	120	RT	39/139 s	135
$Ti_3C_2T_x$/rGO/CuO		Acetone	100	RT	6.5/7.5 s	137
SnO–SnO_2/$Ti_3C_2T_x$		Acetone	100	RT	18/9 s	139
$Ti_3C_2T_x$/SnO_2	HF	Ethanol	10	230 °C	14/26 s	148
Co_3O_4/$Ti_3C_2T_x$	—	Ethanol	50		50/45 s	149
$Ti_3C_2T_x$/WSe_2		Ethanol	40	RT	9.7/6.6 s	147
$Ti_3C_2T_x$/PANI	HF	Ethanol	200	RT	0.4/0.5 s	150
S-$Ti_3C_2T_x$	LiF-HCl	Toluene	10	RT	—	151
$Ti_3C_2T_x$/CuO	HF	Toluene	50	250	270/10 s	152
rGO/N-$Ti_3C_2T_x$/TiO_2	LiF-HCl	Formaldehyde	10	20	27.6/4.8 s	153
$Ti_3C_2T_x$/CO_3O_4	LiF-HCl	Formaldehyde	10	25	83/5 s	154
$ZnSnO_3$/$Ti_3C_2T_x$		Formaldehyde	100	RT	6.2/5.1 s	155
$W_{18}O_{49}$/$Ti_3C_2T_x$		Acetone	170 ppb		5.6/6 s	156
$V_4C_3T_x$ MXene	HF	Acetone	1	25	—	157
α-Fe_2O_3/$Ti_3C_2T_x$		Acetone	5	RT	5/5 s	158
α-/γ-Fe_2O_3/ex-$Ti_3C_2T_x$	Solvothermal	Acetone	100	250	13/8 s	159
1D/2DKWO/$Ti_3C_2T_x$	HF	Acetone		RT	—	160
Nitrogen-doped $Ti_3C_2T_x$	HF	Acetone	—	150	36/9 s	161
Accordion-like $Ti_3C_2T_x$	HF	Acetone	250 ppb	RT	53/120 s	162

 © 2023 The Author(s). Published by the Royal Society of Chemistry

Open Access Article. Published on 25 agosto 2023. Downloaded on 8/8/2025 16:09:06. This article is licensed under a Creative Commons Attribution 3.0 Unported Licence.

sites for gas adsorption. Furthermore, $Ti_3C_2T_x$ MXene-based gas sensors have a very low detection limit of 50–100 ppb for VOCs contaminants at room temperature. Because of its good chemical stability, easy synthesis technique, low cast, and structural variety, $WO_{x\leq 3}$ (tungsten oxide) has received significant attention. $WO_{x\leq 3}$ has a lot of oxygen vacancies, which function as extra-active sites for gas adsorption. $W_{18}O_{49}/Ti_3C_2T_x$ nanocomposites were successfully created by using a simple solvothermal technique for acetone gas sensing to boost sensing performance at lower concentrations. To create the 1D/2D $W_{18}O_{49}/Ti_3C_2T_x$ composite, 1D $W_{18}O_{49}$ nanorods were evenly distributed on 2D $Ti_3C_2T_x$ nanosheets. The $W_{18}O_{49}/Ti_3C_2T_x$ nanocomposite showed a strong response at low concentrations (11.6–20 ppm acetone), great selectivity, short response-recovery times, excellent stability, and a low threshold for detecting acetone (170 ppb) with a response-recovery time of 5.6/6 s, respectively.[156] Most research has been done on $Ti_3C_2T_x$ MXene-based sensors for VOCs gases. Nowadays, the most studied V-based MXene are V_2CT_x, $V_3C_2T_x$, and $V_4C_3T_x$, as reported by W. N. Zho *et al.*[157] The $V_4C_3T_x$ MXene was created by etching the Al layer from the $V_4C_3T_x$ MAX phase in an aqueous HF solution at room temperature. Fig. 9a–d shows SEM pictures that illustrate the changes in structure caused by HF etching, and Fig. 9c–d demonstrates the removal of the Al element from V_4AlC_3. $V_4C_3T_x$ MXene exhibits semiconducting behavior. $V_4C_3T_x$ MXene exhibits the highest overall performance for acetone, including low temperature (25 °C), strong selectivity, good ideal operating sensitivity, and short response-recovery time with a LOD of 1 ppm. According to Fig. 9n–q, this makes the $V_4C_3T_x$ sensor suitable as a practical acetone sensor. As a result, the $V_4C_3T_x$-based sensor has a high potential for providing a room-temperature solution for noninvasive diabetes monitoring.

Madeshwari *et al.*[174] reported on a V_2O_5 nanowires-based acetone sensor. Its response/recovery time are 49/19 s for 50 ppm acetone at 30 °C. Sanjit Manohar Maji *et al.*[175] reported on the urchin-like V_2CT_x/V_2O_5 hybrid sensors, which demonstrated fast response/recovery times of 115/180 s for very low acetone detection limit at 250 ppb, and superb reproducibility with long-term stability (21 days) at room temperature. Its increased response is $S(\%) = 11.9$ around 15 ppm at ambient temperature.

W. Q. Li *et al.*[176] reported on the SnO_2 nanobelt as an acetone sensor. Its response/recovery times are 38/9 s for 5 ppm acetone at 260 °C. Zijing Wang *et al.*[139] reported on a hydrothermal technique for the fabrication of $SnO–SnO_2/Ti_3C_2T_x$ composites. By distribution of $SnO–SnO_2$ (p–n junction) nanoparticles on the surface of 2D $Ti_3C_2T_x$ nanosheets, an effective acetone detection sensor was developed. The $SnO–SnO_2/Ti_3C_2T_x$ based sensor exhibited increased acetone sensing responses of 12.1 with response/recovery times of 18/9 s at ambient temperature and an exceptional repeatability. Because of the different work functions, a Schottky barrier was formed between the SnO and $Ti_3C_2T_x$ nanosheets, functioning as a layer of hole accumulation between the two materials.

Shurong Wang *et al.*[177] reported on porous α-Fe_2O_3 hollow microspheres for acetone sensors. It showed response/recovery times of 17/30 s for 100 ppm acetone at 250 °C. Miao Liu *et al.*[158] showed that the α-$Fe_2O_3/Ti_3C_2T_x$ nanocomposite, which was well produced by a simple hydrothermal technique, demonstrated remarkable performance for acetone at ambient temperature. As a result, 250 nm sized α-Fe_2O_3 nanotubes were appropriately dispersed over the surface of a $Ti_3C_2T_x$ nanosheet. The α-$Fe_2O_3/Ti_3C_2T_x$ nanocomposite has a high response of 16.6% for an acetone concentration of 5 ppm, with a response/recovery time of 5/5 s with good linearity and significant repeatability at ambient temperature. Dandan Huang *et al.*[159] reported that at ambient temperature, MOFs created a porous $\alpha/\gamma Fe_2O_3$/ex-$Ti_3C_2T_x$ nanocomposite that performed well as an acetone sensor due to a variety of heterojunction contacts, porosity, and surface defects. Solvothermal and calcination methods were used to produce this material. Here, the surface of the $Ti_3C_2T_x$ nanosheets is evenly covered by bi-phase α-/γ-Fe_2O_3 nanoparticles, which improves the acetone-sensing performance. The α-/γ-Fe_2O_3/ex-$Ti_3C_2T_x$ sensor has a rapid recovery/recovery time of 13/8 s with great repeatability and exceptional selectivity at 255 °C for 100 ppm of acetone.

Obinna Ama *et al.*[160] reported on 1D/2DKWO nanorod/$Ti_3C_2T_x$ nanocomposites for acetone sensing with different compositional ratios for room temperature sensing. KWO/$Ti_3C_2T_x$ showed the best response at a 2 : 1 ratio. Z. Wang *et al.*[161] showed the porous nitrogen-doped $Ti_3C_2T_x$ used as an acetone gas sensor due to its three-dimensional structure, which was synthesized by the sacrificial template method. When heteroatoms such as nitrogen atoms are introduced into $Ti_3C_2T_x$ nanosheets, certain defects are produced throughout the nitrogen atoms, which can improve the hydrophilicity and adsorption characteristics of the $Ti_3C_2T_x$ nanosheet. Therefore, porous nitrogen-doped $Ti_3C_2T_x$ has a good response/recovery time of 36 s/9 s at 150 °C for acetone detection.

Kampara Roopa Kishore *et al.*[178] reported on the CuO nanograin for acetone sensing at an operating temperature of 350 °C. Its response/recovery times are 11/13 s for 693 ppm acetone. M Liu *et al.*[137] reported that when superfine CuO nanoparticles are decorated on 3D $Ti_3C_2T_x$ MXene and rGO (reduce graphene oxide) nanosheets, 3D $Ti_3C_2T_x$/rGO/CuO is formed. Because of the large surface area of the interconnected spongy network, the even dispersion of CuO nanoparticles, and the excellent electrical conductivity of 3D MXene/rGO/CuO, the sensing performance of acetone at room temperature is high, with a response-recovery time of 6.5 s/7.5 s for 100 ppm acetone, as well as good reproducibility and selectivity. Sanjit at al.[162] presented the accordion-like $Ti_3C_2T_x$ MXene, which was created using a suitable HF etching method at 60 °C for acetone vapor detection as a chemiresistive gas sensor. SEM images of the accordion-like $Ti_3C_2T_x$ are exhibited in Fig. 10a and b, and EDS measurements of various functional groups are given in Fig. 10c–g. Fig. 10h and i are the TEM images of $Ti_3C_2T_x$, which indicate the presence of few-layered MXene flakes. Fig. 10j shows an XRD graph with a shifting peak at a lower angle (002). With p-type sensing characteristics, the sensor successfully identified acetone vapors at ppb levels. The sensing graph is displayed in Fig. 10k–n, with a satisfactory reaction time of 53 s and an acetone detection limit of roughly 250 ppb. At 23 °C, the sensor has great repeatability, long-term stability,

Open Access Article. Published on 25 agosto 2023. Downloaded on 8/8/2025 16:09:06.
This article is licensed under a Creative Commons Attribution 3.0 Unported Licence.

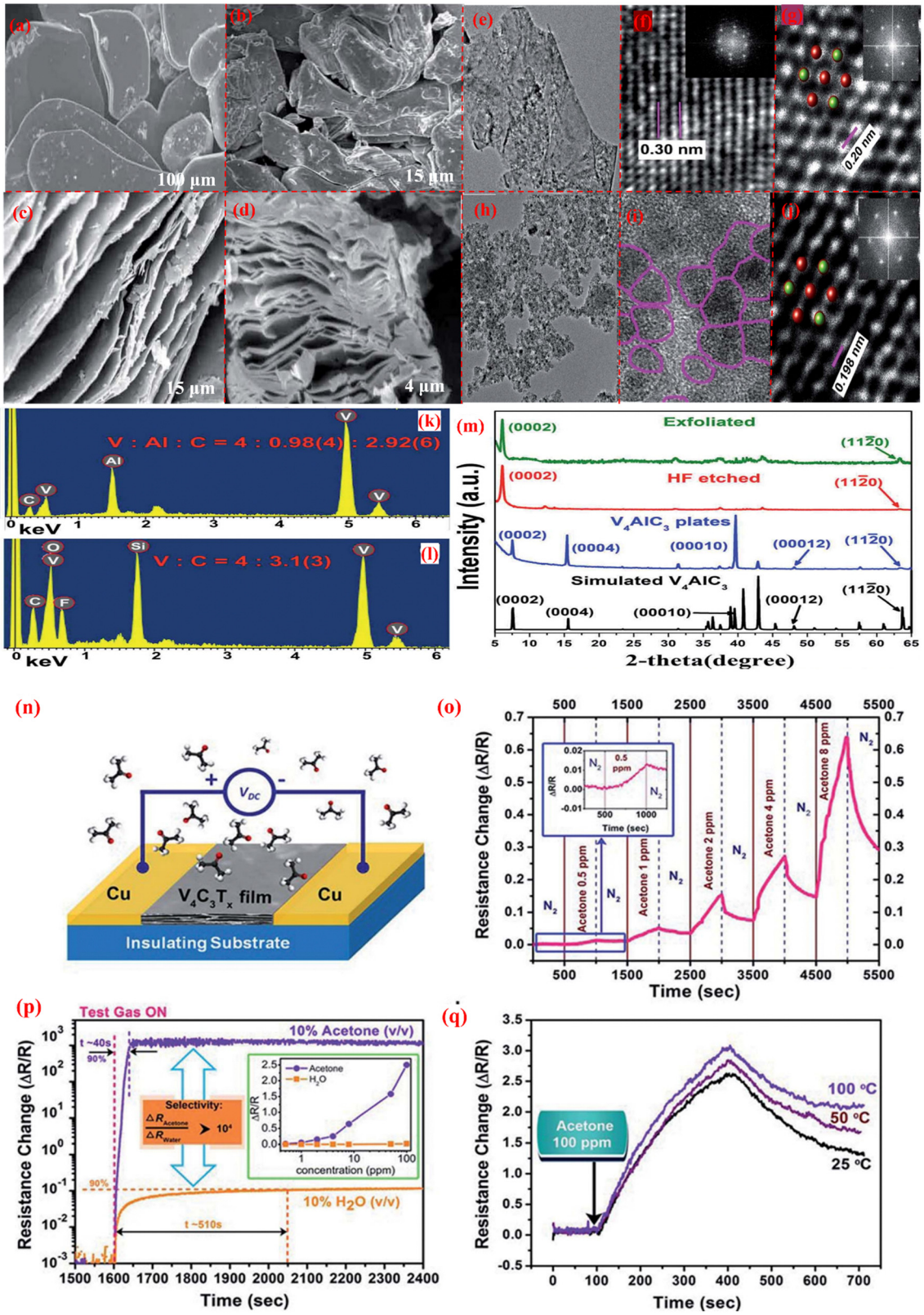

Fig. 9 Characterization and investigation of the V_4AlC_3 MAX phase before and after etching with HF. (a) SEM image of the synthesized V_4AlC_3 plates. (b)–(d) Different magnification SEM images of V_4AlC_3 after HF (48% concertation) treatment. (e)–(j) TEM characterization of thin layer exfoliated V_4AlC_3 nanosheets: high-resolution TEM image, TEM with atomic resolution at Z contrast STEM, corresponding FET pattern and image of $V_4C_3T_x$ at low magnification, high-resolution image, TEM image and STEM. (k and l) EDS measurement for the surface of V_4AlC_3 above SiO_2/Si and $V_4C_3T_x$ surface. (m) XRD characteristics of V_4AlC_3 before and after HF etching. (n) Fabricated $V_4C_3T_x$ film sensor above an insulating substrate with a copper electrode for mechanical support. (o) Sensor response of the $V_4C_3T_x$ film at various concentrations of acetone for acetone sensing. (p) Comparison of the sensing response of the $V_4C_3T_x$ film between acetone and water vapor. (q) Gas-sensing response of the $V_4C_3T_x$ film at various temperatures; reprinted ref. 157. Copyright RSC Advances.

 © 2023 The Author(s). Published by the Royal Society of Chemistry

Open Access Article. Published on 25 agosto 2023. Downloaded on 8/8/2025 16:09:06.
This article is licensed under a Creative Commons Attribution 3.0 Unported Licence.

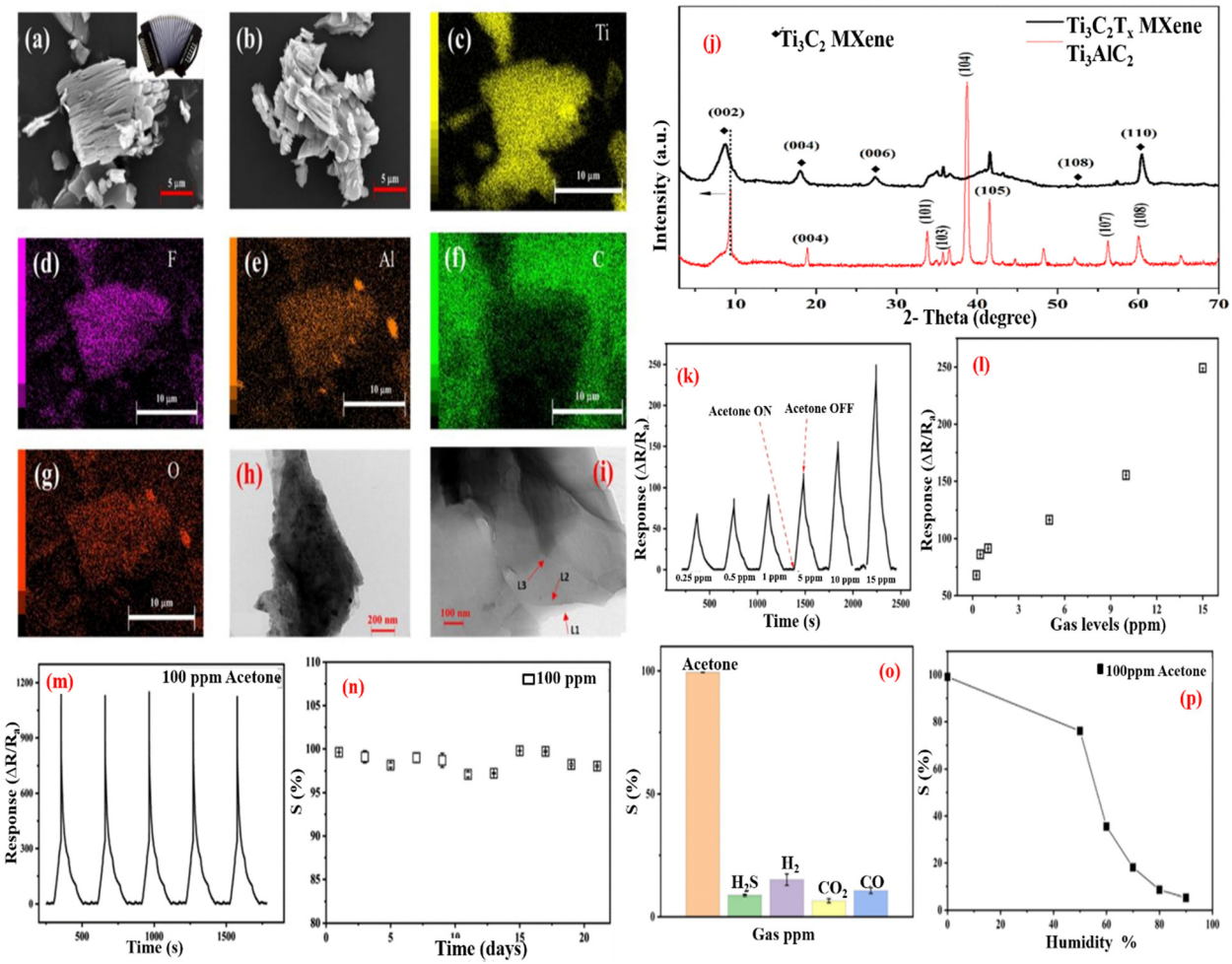

Fig. 10 (a) and (b) SEM images of the exfoliated $Ti_3C_2T_x$ MXene. (c)–(g) Related EDS elemental design of the $Ti_3C_2T_x$ MXene exhibits Ti, Al, F, O, and C elements. (h)–(i) TEM images of the $Ti_3C_2T_x$ MXene, representative of the few-layers MXene flakes. (j) XRD pattern of TI_3AlC_2 before and after HF treatment. (k) Sensing response of the Ti_3CT_x MXene sensor at various concentrations of acetone at RT. (l) Sensing response at a concentration of acetone gas levels (0.24–15 ppm). (m) and (n) Repeatability and stability test of the Ti_3CT_x MXene-based gas sensor for 100 ppm acetone at 23 °C. (o) Response nature of the Ti_3CT_x MXene gas sensor for 100 ppm of different gases. (p) Sensing response of the Ti_3CT_x MXene-based gas sensor as a function of RHs. Reprinted ref. 162. Copyright Applied Electronic Material ACS.

and strong acetone vapor selectivity. As a breath sensor, it offers a lot of potential for diabetic patients because the MXene surface functional groups are chemically reactive and can be functionalized.

6. Other applications of MXene

MXenes have attracted much attention as a unique member of the 2D material family, and researchers are continuing to study its abundant composition, characteristics, and structure of 2D transition metal carbides, nitrides, and carbonitrides. The large surface area, surface functionalization, great hydrophilicity, high conductivity, outstanding optical characteristics, and biocompatibility are just a few unique characteristics of MXene, and they may be employed successfully in a variety of applications, as explained in Fig. 11. For instance, the outstanding optical and electrical properties of 2D MXenes may be exploited to create sensors.[179] MXenes have been hugely studied as electrode materials for different types of rechargeable batteries (Li, K, and Na-ions), electromagnetic interface shields, photothermal conversion, water treatment, hydrogen storage, and supercapacitor, and other applications. MXenes have tremendous potential for usage as an electrode material for supercapacitor applications due to its high electrical conductivity and wide surface chemistry. It was found that $Ti_3C_2T_x$ MXene was perhaps intercalated automatically using cations like NH^{4+}, K^+, Al^+, Na^+, and Mg^{2+} in related salt solutions.[180] Sun *et al.* used 2D Ti_3C_2 MXene obtained after intercalation with DMSO, focusing on the production of anode materials for Li^+ batteries. The electrochemical performance of the intercalated 2D Ti_3C_2 MXene is much higher than that of 2D Ti_3C_2 with groups –F terminated.[181] In electrocatalysis and photocatalysis, MXene exhibits attractive chemical properties due to its superb electroconductivity, functionalization, and durability. Only limited catalytic reactions have been reported with MXene like CO oxidation,[182] oxygen reduction reaction,[183]

Open Access Article. Published on 25 agosto 2023. Downloaded on 8/8/2025 16:09:06.
This article is licensed under a Creative Commons Attribution 3.0 Unported Licence.

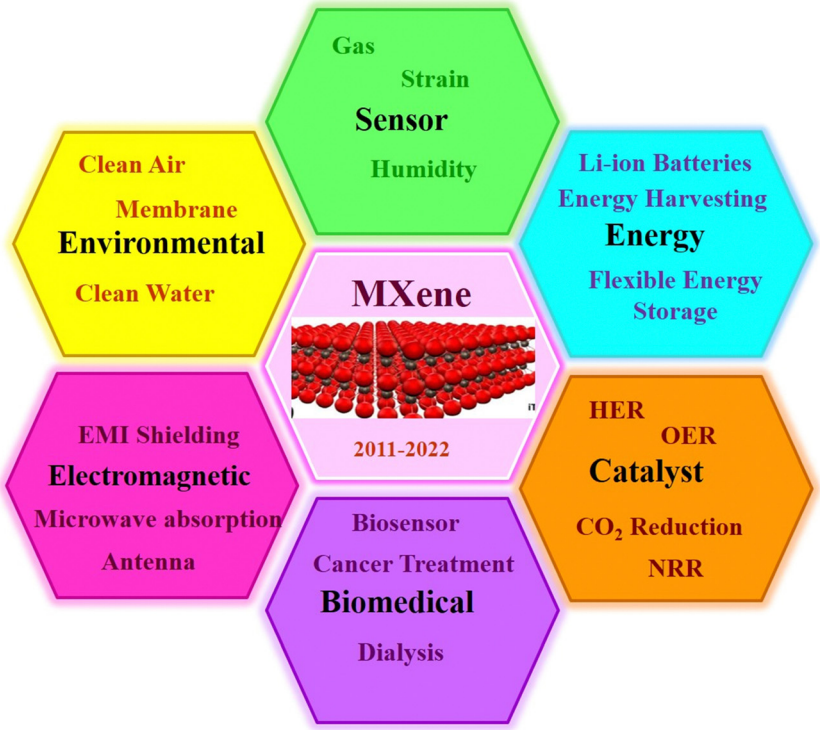

Fig. 11 Schematic diagram illustrating the uses of MXene in different fields.

dehydration of hydrogen storage materials,[184] oxygen evolution reaction,[90] and the hydrogen evolution reaction.[185] In all of these reactions, MXene behaves as a catalyst, supporting substance, and co-catalyst. As for hydrogen storage material, the catalysts should have the following important properties: high cycle stability, and low dehydrogenation temperature. Zhou *et al.* reported on the synthesis of $Ti_3C_2(OH_xF_{1-x})$ and $A_{0.9}R_{0.1}$–TiO_2/C materials, which exhibited anomalous catalytic activity for the dehydrogenation of $NaAlH_4$. The materials demonstrated a capacity of 3.08 wt% in 240 minutes at 90 °C and 85 minutes at 100 °C, and were stable for 10 cycles.[184] Fan and his group coated $Ti_3C_2X_2$ with Ru nanoparticles with a 2.4 nm particle size, and this composite easily catalyzed the hydrolysis of $NaBH_4$ at ambient temperature.[186] According to a measured investigation, the optimal catalyst concentration is 6.99 wt% for a high hydrogen generation rate of 59.04 LH_2 g_{Ru}^{-1} min^{-1}.[186] MXene has both metallic conductivity and hydrophilic surface characteristics, so it is good for electromagnetic interference shielding applications. Due to the 2D MXene structure, the high electrical conductivity and electronic coupling between layers are responsible for better EMI (Elctro-Magnetic Interference) shielding.[88]

7. Conclusions

A history on the progress of 2D MXene materials, an explanation of how MXene is created from the MAX phase by selective etching with the proper etchant and a delaminating agent, and a comparison of the two states using morphology and XRD patterns show that MXene is the better candidate among all 2D materials. Along with their suitability for gas sensing, 2D MXene-based materials have several positive attributes, such as improved functional groups, a high surface-to-volume ratio, superior electrical, mechanical, chemical, and adjustable band gap capabilities, outstanding stability, and enhanced functional groups. A substantial amount of research on MXene nanocomposite-based VOC sensors has been conducted and is reported in this study. MXene-based materials have proven their particular advantage in biological sensing applications, with a focus on the most recent advancements in pure MXene and their nanocomposite-based acetone gas sensor. Finally, it has been explained how MXene nanocomposite detects ppb level acetone at ambient temperature, and how the related sensing performance summarizes the applicability of MXene in numerous sectors.

Conflicts of interest

The authors declare that they have no known competing financial interests or personal relationships that could have appeared to influence the work reported in this paper.

Acknowledgements

Monu Gupta acknowledges Babasaheb Bhimrao Ambedkar University, Lucknow, UP, India for providing a UGC non-NET fellowship. Mr Arpit Verma and the corresponding author Prof. B. C. Yadav acknowledge the Uttar Pradesh Council of Science

 © 2023 The Author(s). Published by the Royal Society of Chemistry

Open Access Article. Published on 25 agosto 2023. Downloaded on 8/8/2025 16:09:06.
This article is licensed under a Creative Commons Attribution 3.0 Unported Licence.

and Technology, Lucknow for financial assistance in the form of Project Ref: CST/D-2290.

References

1 R. Bhardwaj and A. Hazra, *J. Mater. Chem. C*, 2021, **9**, 15735–15754.
2 S. Yang, C. Jiang and S. Wei, *Appl. Phys. Rev.*, 2017, **4**, 21304.
3 H. Zhang and R. Lv, *J. Mater.*, 2018, **4**, 95–107.
4 C. Choi, Y. Lee, K. W. Cho, J. H. Koo and D.-H. Kim, *Acc. Chem. Res.*, 2018, **52**, 73–81.
5 A. Mirzaei, S. G. Leonardi and G. Neri, *Ceram. Int.*, 2016, **42**, 15119–15141.
6 N. Joshi, T. Hayasaka, Y. Liu, H. Liu, O. N. Oliveira and L. Lin, *Microchim. Acta*, 2018, **185**, 1–16.
7 S. Pirsa and N. Alizadeh, *Sens. Actuators, B*, 2010, **147**, 461–466.
8 M. Masikini, M. Chowdhury and O. Nemraoui, *J. Electrochem. Soc.*, 2020, **167**, 37537.
9 X. Cai, Y. Luo, B. Liu and H.-M. Cheng, *Chem. Soc. Rev.*, 2018, **47**, 6224–6266.
10 V. M. H. Ng, H. Huang, K. Zhou, P. S. Lee, W. Que, J. Z. Xu and L. B. Kong, *J. Mater. Chem. A*, 2017, **5**, 3039–3068.
11 W. E. O. Ghoma, H. Sevik and K. Isinkaralar, *Air Qual. Atmos. Heal.*, 2022, **15**, 415–424.
12 A. V. Tyurnina, I. Tzanakis, J. Morton, J. Mi, K. Porfyrakis, B. M. Maciejewska, N. Grobert and D. G. Eskin, *Carbon*, 2020, **168**, 737–747.
13 L. Xuan, Y. Ma, Y. Xing, Q. Meng, J. Song, T. Chen, H. Wang, P. Wang, Y. Zhang and P. Gao, *Environ. Pollut.*, 2021, **270**, 116074.
14 S. H. Cho, J. M. Suh, T. H. Eom, T. Kim and H. W. Jang, *Electron. Mater. Lett.*, 2021, **17**, 1–17.
15 P. Srinivasan, A. J. Kulandaisamy, G. K. Mani, K. J. Babu, K. Tsuchiya and J. B. B. Rayappan, *RSC Adv.*, 2019, **9**, 30226–30239.
16 S. Singh, U. Kumar, B. C. Yadav, K. Kumar, R. K. Tripathi and K. Singh, *Results Phys.*, 2019, **15**, 102772.
17 A. S. Manolis, T. A. Manolis and A. A. Manolis, *Int. J. Mol. Sci.*, 2023, **24**, 3534.
18 N. H. Cho, J. E. Shaw, S. Karuranga, Y. Huang, J. D. da Rocha Fernandes, A. W. Ohlrogge and B. Malanda, *Diabetes Res. Clin. Pract.*, 2018, **138**, 271–281.
19 F. Chen, M. Yang, X. Wang, Y. Song, L. Guo, N. Xie, X. Kou, X. Xu, Y. Sun and G. Lu, *Sens. Actuators, B*, 2019, **290**, 459–466.
20 K. Pathak, R. Saikia, H. Sarma, M. P. Pathak, R. J. Das, U. Gogoi, M. Z. Ahmad, A. Das and B. A. A. Wahab, *J. Diabetes Metab. Disord.*, 2023, 1–15.
21 M. S. Sha, M. R. Maurya, S. Shafath, J.-J. Cabibihan, A. Al-Ali, R. A. Malik and K. K. Sadasivuni, *ACS Omega*, 2022, **7**, 4257–4266.
22 H. R. Ansari, A. Mirzaei, H. Shokrollahi, R. Kumar, J.-Y. Kim, H. W. Kim, M. Kumar and S. S. Kim, *J. Mater. Chem. C*, 2023, 6528–6549.
23 V. Longo, A. Forleo, A. Ferramosca, T. Notari, S. Pappalardo, P. Siciliano, S. Capone and L. Montano, *Environ. Pollut.*, 2021, **286**, 117410.
24 S. Halder, Z. Xie, M. H. Nantz and X.-A. Fu, *J. Chromatogr. A*, 2022, **1673**, 463083.
25 A. Singh, S. Sikarwar, A. Verma and B. C. Yadav, *Sens. Actuators, A*, 2021, **332**, 113127.
26 M. Catelani, L. Ciani and M. Venzi, *Reliab. Eng. Syst. Saf.*, 2018, **180**, 425–433.
27 K. Rana and R. K. Sonker, *Smart Nanostructure Materials and Sensor Technology*, Springer, 2022, pp. 179–199.
28 A. Verma, D. Yadav, A. Singh, M. Gupta, K. B. Thapa and B. C. Yadav, *Sens. Actuators, B*, 2022, **361**, 131708.
29 B. K. S. Reddy and P. H. Borse, *J. Electrochem. Soc.*, 2021, **168**, 57521.
30 H. Teymourian, F. Tehrani, K. Mahato and J. Wang, *Adv. Healthcare Mater.*, 2021, **10**, 2002255.
31 J. Wang, H. Shen, Y. Xia and S. Komarneni, *Ceram. Int.*, 2021, **47**, 7353–7368.
32 T. Chen, T. Liu, T. Li, H. Zhao and Q. Chen, *Clin. Chim. Acta*, 2021, **515**, 61–72.
33 D. J. Buckley, N. C. G. Black, E. G. Castanon, C. Melios, M. Hardman and O. Kazakova, *2D Mater.*, 2020, **7**, 32002.
34 V. Amiri, H. Roshan, A. Mirzaei, G. Neri and A. I. Ayesh, *Sensors*, 2020, **20**, 3096.
35 S. J. Ward, R. Layouni, S. Arshavsky-Graham, E. Segal and S. M. Weiss, *ACS Sens.*, 2021, **6**, 2967–2978.
36 T. Rasheed, *Mater. Today Chem.*, 2022, **24**, 100859.
37 D. H. Ho, Y. Y. Choi, S. B. Jo, J.-M. Myoung and J. H. Cho, *Adv. Mater.*, 2021, **33**, 2005846.
38 H. Riazi, G. Taghizadeh and M. Soroush, *ACS omega*, 2021, **6**, 11103–11112.
39 X. Liu, T. Ma, N. Pinna and J. Zhang, *Adv. Funct. Mater.*, 2017, **27**, 1702168.
40 J.-K. Qin, C. Wang, L. Zhen, L.-J. Li, C.-Y. Xu and Y. Chai, *Prog. Mater. Sci.*, 2021, **122**, 100856.
41 D. S. Schulman, A. J. Arnold and S. Das, *Chem. Soc. Rev.*, 2018, **47**, 3037–3058.
42 C. Cui, F. Xue, W.-J. Hu and L.-J. Li, *npj 2D Mater. Appl.*, 2018, **2**, 1–14.
43 X. Zhang, Y. Nie, Q. Zhang, Z. Liang, P. Wang and Q. Ma, *Chem. Eng. J.*, 2021, **411**, 128428.
44 Y. Li, Y.-L. Li, B. Sa and R. Ahuja, *Catal. Sci. Technol.*, 2017, **7**, 545–559.
45 G. Neri, *Chemosensors*, 2017, **5**, 21.
46 M. Ko, L. Mendecki and K. A. Mirica, *Chem. Commun.*, 2018, **54**, 7873–7891.
47 S.-T. Han, H. Peng, Q. Sun, S. Venkatesh, K.-S. Chung, S. C. Lau, Y. Zhou and V. A. L. Roy, *Adv. Mater.*, 2017, **29**, 1700375.
48 S. Rana, V. Singh and B. Singh, *iScience*, 2022, 103748.
49 K. Khan, A. K. Tareen, M. Iqbal, L. Wang, C. Ma, Z. Shi, Z. Ye, W. Ahmad, R. U. R. Sagar and S. S. Shams, *et al.*, *Prog. Solid State Chem.*, 2021, **63**, 100326.
50 D. Cheng, P. Li, X. Zhu, M. Liu, Y. Zhang and Y. Liu, *Chin. J. Chem.*, 2021, **39**, 2181–2187.

© 2023 The Author(s). Published by the Royal Society of Chemistry

Open Access Article. Published on 25 agosto 2023. Downloaded on 8/8/2025 16:09:06.
This article is licensed under a Creative Commons Attribution 3.0 Unported Licence.

51 J. Barman, A. Tirkey, S. Batra, A. A. Paul, K. Panda, R. Deka and P. J. Babu, *Mater. Today Commun.*, 2022, **32**, 104055.
52 B. Xu, C. Zhi and P. Shi, *J. Phys. Mater.*, 2020, **3**, 31001.
53 M. Dahlqvist, J. Lu, R. Meshkian, Q. Tao, L. Hultman and J. Rosen, *Sci. Adv.*, 2017, **3**, e1700642.
54 S. K. Hwang, S.-M. Kang, M. Rethinasabapathy, C. Roh and Y. S. Huh, *Chem. Eng. J.*, 2020, **397**, 125428.
55 P. E. Lokhande, A. Pakdel, H. M. Pathan, D. Kumar, D.-V. N. Vo, A. Al-Gheethi, A. Sharma, S. Goel, P. P. Singh and B.-K. Lee, *Chemosphere*, 2022, **297**, 134225.
56 Y. Wang, T. Guo, Z. Tian, K. Bibi, Y.-Z. Zhang and H. N. Alshareef, *Adv. Mater.*, 2022, **34**, 2108560.
57 R. Khan and S. Andreescu, *Sensors*, 2020, **20**, 5434.
58 B. Anasori, M. R. Lukatskaya and Y. Gogotsi, *Nat. Rev. Mater.*, 2017, **2**, 1–17.
59 C. Lamiel, I. Hussain, O. R. Ogunsakin and K. Zhang, *J. Mater. Chem. A*, 2022, 14247–14272.
60 Q. Zhang, Y. Sun, M. Liu and Y. Liu, *Nanoscale*, 2020, **12**, 1826–1832.
61 S. De, S. Acharya, S. Sahoo and G. C. Nayak, *Mater. Chem. Front.*, 2021, **5**, 7134–7169.
62 M. Alhabeb, K. Maleski, B. Anasori, P. Lelyukh, L. Clark, S. Sin and Y. Gogotsi, *Chem. Mater.*, 2017, **29**, 7633–7644.
63 B. Anasori, Y. Xie, M. Beidaghi, J. Lu, B. C. Hosler, L. Hultman, P. R. C. Kent, Y. Gogotsi and M. W. Barsoum, *ACS Nano*, 2015, **9**, 9507–9516.
64 A. Petruhins, J. Lu, L. Hultman and J. Rosen, *Mater. Res. Lett.*, 2019, **7**, 446–452.
65 G. R. Bhimanapati, Z. Lin, V. Meunier, Y. Jung, J. Cha, S. Das, D. Xiao, Y. Son, M. S. Strano and V. R. Cooper, *et al.*, *ACS Nano*, 2015, **9**, 11509–11539.
66 T. Tan, X. Jiang, C. Wang, B. Yao and H. Zhang, *Adv. Sci.*, 2020, **7**, 2000058.
67 R. A. Soomro, S. Jawaid, Q. Zhu, Z. Abbas and B. Xu, *Chin. Chem. Lett.*, 2020, **31**, 922–930.
68 Q. Li, Y. Li and W. Zeng, *Chemosensors*, 2021, **9**, 225.
69 Y. Ibrahim, A. Mohamed, A. M. Abdelgawad, K. Eid, A. M. Abdullah and A. Elzatahry, *Nanomaterials*, 2020, **10**, 1916.
70 M. Naguib, V. N. Mochalin, M. W. Barsoum and Y. Gogotsi, *Adv. Mater.*, 2014, **26**, 982.
71 L. Verger, C. Xu, V. Natu, H.-M. Cheng, W. Ren and M. W. Barsoum, *Curr. Opin. Solid State Mater. Sci.*, 2019, **23**, 149–163.
72 E. Lee and D.-J. Kim, *J. Electrochem. Soc.*, 2019, **167**, 37515.
73 A. N. Enyashin and A. L. Ivanovskii, *Comput. Theor. Chem.*, 2012, **989**, 27–32.
74 S. Mehdi Aghaei, A. Aasi and B. Panchapakesan, *ACS Omega*, 2021, **6**, 2450–2461.
75 J. Zou, J. Wu, Y. Wang, F. Deng, J. Jiang, Y. Zhang, S. Liu, N. Li, H. Zhang and J. Yu, *et al.*, *Chem. Soc. Rev.*, 2022, **51**, 2972–2990.
76 K. Hantanasirisakul and Y. Gogotsi, *Adv. Mater.*, 2018, **30**, 1804779.
77 W. Sun, Y. Xie and P. R. C. Kent, *Nanoscale*, 2018, **10**, 11962–11968.
78 M. Magnuson and M. Mattesini, *Thin Solid Films*, 2017, **621**, 108–130.
79 Y. Yin, L. Shi, S. Zhang, X. Duan, J. Zhang, H. Sun and S. Wang, *Nano Mater. Sci.*, 2023, **1**, 15–38.
80 C. Ougherb, T. Ouahrani, M. Badawi and Á. Morales-García, *Phys. Chem. Chem. Phys.*, 2022, **24**, 7243–7252.
81 A. Iqbal, J. Hong, T. Y. Ko and C. M. Koo, *Nano Converge.*, 2021, **8**, 1–22.
82 Y. Zhang, L. Wang, N. Zhang and Z. Zhou, *RSC Adv.*, 2018, **8**, 19895–19905.
83 V. N. Borysiuk, V. N. Mochalin and Y. Gogotsi, *Comput. Mater. Sci.*, 2018, **143**, 418–424.
84 Z. Lu, Y. Wei, J. Deng, L. Ding, Z.-K. Li and H. Wang, *ACS Nano*, 2019, **13**, 10535–10544.
85 M. Benchakar, L. Loupias, C. Garnero, T. Bilyk, C. Morais, C. Canaff, N. Guignard, S. Morisset, H. Pazniak and S. Hurand, *et al.*, *Appl. Surf. Sci.*, 2020, **530**, 147209.
86 S. Munir, A. Rasheed, T. Rasheed, I. Ayman, S. Ajmal, A. Rehman, I. Shakir, P. O. Agboola and M. F. Warsi, *ACS Omega*, 2020, **5**, 26845–26854.
87 D. Xiong, X. Li, Z. Bai and S. Lu, *Small*, 2018, **14**, 1703419.
88 F. Shahzad, M. Alhabeb, C. B. Hatter, B. Anasori, S. Man Hong, C. M. Koo and Y. Gogotsi, *Science*, 2016, **353**, 1137–1140.
89 K. A. A. Usman, S. Qin, L. C. Henderson, J. Zhang, D. Hegh and J. M. Razal, *Mater. Horiz.*, 2021, **8**, 2886–2912.
90 T. Y. Ma, J. L. Cao, M. Jaroniec and S. Z. Qiao, *Angew. Chem., Int. Ed.*, 2016, **55**, 1138–1142.
91 S. Qamar, K. Fatima, N. Ullah, Z. Akhter, A. Wasim and M. S. Sultan, *Nanoscale*, 2022, **14**, 13018–13039.
92 N. R. Hemanth and B. Kandasubramanian, *Chem. Eng. J.*, 2020, **392**, 123678.
93 Y.-Z. Zhang, Y. Wang, Q. Jiang, J. K. El-Demellawi, H. Kim and H. N. Alshareef, *Adv. Mater.*, 2020, **32**, 1908486.
94 Y. Lee, Y. Hwang, S. B. Cho and Y.-C. Chung, *Phys. Chem. Chem. Phys.*, 2014, **16**, 26273–26278.
95 B. Anasori, C. Shi, E. J. Moon, Y. Xie, C. A. Voigt, P. R. C. Kent, S. J. May, S. J. L. Billinge, M. W. Barsoum and Y. Gogotsi, *Nanoscale Horiz.*, 2016, **1**, 227–234.
96 M. Naguib, M. Kurtoglu, V. Presser, J. Lu, J. Niu, M. Heon, L. Hultman, Y. Gogotsi and M. W. Barsoum, *Adv. Mater.*, 2011, **23**, 4248–4253.
97 B. Anasori and Y. Gogotsi, *2D Metal carbides and nitrides (MXenes)*, Springer, 2019, pp. 3–12.
98 M. Naguib, O. Mashtalir, J. Carle, V. Presser, J. Lu, L. Hultman, Y. Gogotsi and M. W. Barsoum, *ACS Nano*, 2012, **6**, 1322–1331.
99 O. Salim, K. A. Mahmoud, K. K. Pant and R. K. Joshi, *Mater. Today Chem.*, 2019, **14**, 100191.
100 M. K. Aslam and M. Xu, *Nanoscale*, 2020, **12**, 15993–16007.
101 C. Zhang, M. Beidaghi, M. Naguib, M. R. Lukatskaya, M.-Q. Zhao, B. Dyatkin, K. M. Cook, S. J. Kim, B. Eng and X. Xiao, *et al.*, *Chem. Mater.*, 2016, **28**, 3937–3943.
102 J. Zhou, X. Zha, X. Zhou, F. Chen, G. Gao, S. Wang, C. Shen, T. Chen, C. Zhi and P. Eklund, *et al.*, *ACS Nano*, 2017, **11**, 3841–3850.
103 M. Ghidiu, M. R. Lukatskaya, M.-Q. Zhao, Y. Gogotsi and M. W. Barsoum, *Nature*, 2014, **516**, 78–81.

 © 2023 The Author(s). Published by the Royal Society of Chemistry

Open Access Article. Published on 25 agosto 2023. Downloaded on 8/8/2025 16:09:06.
This article is licensed under a Creative Commons Attribution 3.0 Unported Licence.

104 J. Zhu, E. Ha, G. Zhao, Y. Zhou, D. Huang, G. Yue, L. Hu, N. Sun, Y. Wang and L. Y. S. Lee, *et al.*, *Coord. Chem. Rev.*, 2017, **352**, 306–327.
105 M. Wu, Y. He, L. Wang, Q. Xia and A. Zhou, *J. Adv. Ceram.*, 2020, **9**, 749–758.
106 Y. Guo, S. Jin, L. Wang, P. He, Q. Hu, L.-Z. Fan and A. Zhou, *Ceram. Int.*, 2020, **46**, 19550–19556.
107 Y. Gong, X. Xing, Y. Wang, Z. Lv, Y. Zhou and S.-T. Han, *Small Sci.*, 2021, **1**, 2100006.
108 X. Zhan, C. Si, J. Zhou and Z. Sun, *Nanoscale Horiz.*, 2020, **5**, 235–258.
109 M. Naguib, J. Halim, J. Lu, K. M. Cook, L. Hultman, Y. Gogotsi and M. W. Barsoum, *J. Am. Chem. Soc.*, 2013, **135**, 15966–15969.
110 J. Zhou, X. Zha, F. Y. Chen, Q. Ye, P. Eklund, S. Du and Q. Huang, *Angew. Chem., Int. Ed.*, 2016, **55**, 5008–5013.
111 J. Halim, S. Kota, M. R. Lukatskaya, M. Naguib, M.-Q. Zhao, E. J. Moon, J. Pitock, J. Nanda, S. J. May and Y. Gogotsi, *et al.*, *Adv. Funct. Mater.*, 2016, **26**, 3118–3127.
112 R. Meshkian, M. Dahlqvist, J. Lu, B. Wickman, J. Halim, J. Thörnberg, Q. Tao, S. Li, S. Intikhab and J. Snyder, *et al.*, *Adv. Mater.*, 2018, **30**, 1706409.
113 J. Halim, M. R. Lukatskaya, K. M. Cook, J. Lu, C. R. Smith, L.-Å. Näslund, S. J. May, L. Hultman, Y. Gogotsi and P. Eklund, *et al.*, *Chem. Mater.*, 2014, **26**, 2374–2381.
114 C. Verma and K. K. Thakur, *Eur. J. Mol. Clin. Med.*, 2020, **7**, 4429–4450.
115 M. Naguib, R. R. Unocic, B. L. Armstrong and J. Nanda, *Dalton Trans.*, 2015, **44**, 9353–9358.
116 O. Mashtalir, M. Naguib, V. N. Mochalin, Y. Dall'Agnese, M. Heon, M. W. Barsoum and Y. Gogotsi, *Nat. Commun.*, 2013, **4**, 1–7.
117 Y. Zhang, J. Cao, Z. Yuan, L. Zhao, L. Wang and W. Han, *J. Colloid Interface Sci.*, 2021, **599**, 109–118.
118 K. Maleski, V. N. Mochalin and Y. Gogotsi, *Chem. Mater.*, 2017, **29**, 1632–1640.
119 Q. Zhang, H. Lai, R. Fan, P. Ji, X. Fu and H. Li, *ACS Nano*, 2021, **15**, 5249–5262.
120 Z. Ling, C. E. Ren, M.-Q. Zhao, J. Yang, J. M. Giammarco, J. Qiu, M. W. Barsoum and Y. Gogotsi, *Proc. Natl. Acad. Sci. U. S. A.*, 2014, **111**, 16676–16681.
121 M. Naguib, T. Saito, S. Lai, M. S. Rager, T. Aytug, M. P. Paranthaman, M.-Q. Zhao and Y. Gogotsi, *RSC Adv.*, 2016, **6**, 72069–72073.
122 R. B. Rakhi, P. Nayak, C. Xia and H. N. Alshareef, *Sci. Rep.*, 2016, **6**, 1–10.
123 J. Wang, S. Dong, H. Li, Z. Chen, S. Jiang, L. Wu and X. Zhang, *J. Electroanal. Chem.*, 2018, **810**, 27–33.
124 C. Zhang, *Adv. Funct. Mater.*, 2016, **26**, 4143–4151.
125 F. Mohajer, G. M. Ziarani, A. Badiei, S. Iravani and R. S. Varma, *Nanomaterials*, 2023, **13**, 345.
126 Y. Qian, J. Zhong and J. Ou, *Carbon N. Y.*, 2022, **190**, 104–114.
127 N. C. Popa, *J. Appl. Crystallogr.*, 1992, **25**, 611–616.
128 H.-W. Wang, M. Naguib, K. Page, D. J. Wesolowski and Y. Gogotsi, *Chem. Mater.*, 2016, **28**, 349–359.
129 A. S. Levitt, M. Alhabeb, C. B. Hatter, A. Sarycheva, G. Dion and Y. Gogotsi, *J. Mater. Chem. A*, 2019, **7**, 269–277.
130 W. Guo, S. G. Surya, V. Babar, F. Ming, S. Sharma, H. N. Alshareef, U. Schwingenschlogl and K. N. Salama, *ACS Appl. Mater. Interfaces*, 2020, **12**, 57218–57227.
131 D. E. Newbury and N. W. M. Ritchie, *Scanning*, 2013, **35**, 141–168.
132 W. Yuan, K. Yang, H. Peng, F. Li and F. Yin, *J. Mater. Chem. A*, 2018, **6**, 18116–18124.
133 A. Junkaew and R. Arroyave, *Phys. Chem. Chem. Phys.*, 2018, **20**, 6073–6082.
134 D. Li, G. Liu, Q. Zhang, M. Qu, Y. Q. Fu, Q. Liu and J. Xie, *Sens. Actuators, B*, 2021, **331**, 129414.
135 W. Y. Chen, S.-N. Lai, C.-C. Yen, X. Jiang, D. Peroulis and L. A. Stanciu, *ACS Nano*, 2020, **14**, 11490–11501.
136 H.-J. Koh, S. J. Kim, K. Maleski, S.-Y. Cho, Y.-J. Kim, C. W. Ahn, Y. Gogotsi and H.-T. Jung, *ACS Sens.*, 2019, **4**, 1365–1372.
137 M. Liu, Z. Wang, P. Song, Z. Yang and Q. Wang, *Sens. Actuators, B*, 2021, **340**, 129946.
138 T. He, W. Liu, T. Lv, M. Ma, Z. Liu, A. Vasiliev and X. Li, *Sens. Actuators, B*, 2021, **329**, 129275.
139 Z. Wang, F. Wang, A. Hermawan, Y. Asakura, T. Hasegawa, H. Kumagai, H. Kato, M. Kakihana, J. Zhu and S. Yin, *J. Mater. Sci. Technol.*, 2021, **73**, 128–138.
140 M. Usman, *Membranes*, 2022, **12**, 507.
141 M. Gupta, P. Chaudhary, A. Singh, A. Verma, D. Yadav and B. C. Yadav, *Sens. Actuators, B*, 2022, **368**, 132102.
142 H. G. Shiraz, X. Crispin and M. Berggren, *Int. J. Hydrogen Energy*, 2021, **46**, 24060–24077.
143 R. Malik, V. K. Tomer, Y. K. Mishra and L. Lin, *Appl. Phys. Rev.*, 2020, **7**, 021301.
144 T. Srivastava and R. Jha, *IEEE Photonics Technol. Lett.*, 2018, **30**, 319–322.
145 M. S. Bhargava Reddy, S. Kailasa, B. C. G. Marupalli, K. K. Sadasivuni and S. Aich, *ACS Sens.*, 2022, **7**, 2132–2163.
146 V. Chaudhary, N. Ashraf, M. Khalid, R. Walvekar, Y. Yang, A. Kaushik and Y. K. Mishra, *Adv. Funct. Mater.*, 2022, **32**, 2112913.
147 W. Y. Chen, X. Jiang, S.-N. Lai, D. Peroulis and L. Stanciu, *Nat. Commun.*, 2020, **11**, 1–10.
148 C. Wang, R. Li, L. Feng and J. Xu, *Chemosensors*, 2022, **10**, 109.
149 X. Bu, F. Ma, Q. Wu, H. Wu, Y. Yuan, L. Hu, C. Han, X. Wang, W. Liu and X. Li, *Sens. Actuators, B*, 2022, **369**, 132232.
150 L. Zhao, K. Wang, W. Wei, L. Wang and W. Han, *InfoMat*, 2019, **1**, 407–416.
151 S. N. Shuvo, A. M. Ulloa Gomez, A. Mishra, W. Y. Chen, A. M. Dongare and L. A. Stanciu, *ACS Sens.*, 2020, **5**, 2915–2924.
152 A. Hermawan, B. Zhang, A. Taufik, Y. Asakura, T. Hasegawa, J. Zhu, P. Shi and S. Yin, *ACS Appl. Nano Mater.*, 2020, **3**, 4755–4766.
153 Y. Wang, Y. Zhou and Y. Wang, *Sens. Actuators, B*, 2020, **323**, 128695.
154 D. Zhang, Q. Mi, D. Wang and T. Li, *Sens. Actuators, B*, 2021, **339**, 129923.

Open Access Article. Published on 25 agosto 2023. Downloaded on 8/8/2025 16:09:06.
This article is licensed under a Creative Commons Attribution 3.0 Unported Licence.

155 Z. Sima, P. Song, Y. Ding, Z. Lu and Q. Wang, *Appl. Surf. Sci.*, 2022, 153861.
156 S. Sun, M. Wang, X. Chang, Y. Jiang, D. Zhang, D. Wang, Y. Zhang and Y. Lei, *Sens. Actuators, B*, 2020, **304**, 127274.
157 W. N. Zhao, N. Yun, Z. H. Dai and Y. F. Li, *RSC Adv.*, 2020, **10**, 1261–1270.
158 M. Liu, J. Ji, P. Song, M. Liu and Q. Wang, *Sens. Actuators, B*, 2021, **349**, 130782.
159 D. Huang, H. Li, Y. Wang, X. Wang, L. Cai, W. Fan, Y. Chen, W. Wang, Y. Song and G. Han, *et al.*, *Chem. Eng. J.*, 2022, **428**, 131377.
160 O. Ama, M. Sadiq, M. Johnson, Q. Zhang and D. Wang, *Chemosensors*, 2020, **8**, 102.
161 Z. Wang, F. Wang, A. Hermawan, J. Zhu and S. Yin, *Funct. Mater. Lett.*, 2021, **14**, 2151043.
162 S. M. Majhi, A. Ali, Y. E. Greish, H. F. El-Maghraby, N. N. Qamhieh, A. R. Hajamohideen and S. T. Mahmoud, *ACS Appl. Electron. Mater.*, 2022, **4**, 4094–4103.
163 K. Deshmukh, T. Kovávrik and S. K. K. Pasha, *Coord. Chem. Rev.*, 2020, **424**, 213514.
164 B. Xu, M. Zhu, W. Zhang, X. Zhen, Z. Pei, Q. Xue, C. Zhi and P. Shi, *Adv. Mater.*, 2016, **28**, 3333–3339.
165 Q. Wang, N. Han, Z. Shen, X. Li, Z. Chen, Y. Cao, W. Si, F. Wang, B.-J. Ni and V. K. Thakur, *Nano Mater. Sci.*, 2023, **1**, 35–52.
166 M. AhadiParsa, A. Dehghani, M. Ramezanzadeh and B. Ramezanzadeh, *Adv. Colloid Interface Sci.*, 2022, **307**, 102730.
167 X. Yu, Y. Li, J. Cheng, Z. Liu, Q. Li, W. Li, X. Yang and B. Xiao, *ACS Appl. Mater. Interfaces*, 2015, **7**, 13707–13713.
168 S. Ramanavicius and A. Ramanavicius, *Int. J. Mol. Sci.*, 2020, **21**, 9224.
169 Y. Sun, P. Li, Y. Zhu, X. Zhu, Y. Zhang, M. Liu and Y. Liu, *Biosens. Bioelectron.*, 2021, **194**, 113600.
170 X. Zhu, Y. Zhang, M. Liu and Y. Liu, *Biosens. Bioelectron.*, 2021, **171**, 112730.
171 Z. Xiao, S. Ruan, L. B. Kong, W. Que, K. Zhou, Y. Liu and T. Zhang, *MXenes and MXenes-based Composites*, Springer, 2020, pp. 303–404.
172 F. Wang, C. Yang, C. Duan, D. Xiao, Y. Tang and J. Zhu, *J. Electrochem. Soc.*, 2014, **162**, B16.
173 Y. Xu, T. Ma, L. Zheng, Y. Zhao, X. Liu and J. Zhang, *Sens. Actuators, B*, 2019, **288**, 432–441.
174 M. Ezhilan, J. B. B. Arockia Jayalatha and J. B. B. Rayappan, *Mater. Res. Bull.*, 2021, **139**, 111276.
175 S. M. Majhi, A. Ali, Y. E. Greish, H. F. El-Maghraby and S. T. Mahmoud, *Sci. Rep.*, 2023, **13**, 3114.
176 W. Q. Li, S. Y. Ma, J. Luo, Y. Z. Mao, L. Cheng, D. J. Gengzang, X. L. Xu and S. H. Yan, *Mater. Lett.*, 2014, **132**, 338–341.
177 S. Wang, L. Wang, T. Yang, X. Liu, J. Zhang, B. Zhu, S. Zhang, W. Huang and S. Wu, *J. Solid State Chem.*, 2010, **183**, 2869–2876.
178 K. Roopa Kishore, D. Balamurugan and B. G. Jeyaprakash, *J. Mater. Sci.: Mater. Electron.*, 2021, **32**, 1204–1220.
179 S. K. Bhardwaj, H. Singh, M. Khatri, K.-H. Kim and N. Bhardwaj, *Biosens. Bioelectron.*, 2022, **202**, 113995.
180 M. Hu, Z. Li, T. Hu, S. Zhu, C. Zhang and X. Wang, *ACS Nano*, 2016, **10**, 11344–11350.
181 D. Sun, M. Wang, Z. Li, G. Fan, L.-Z. Fan and A. Zhou, *Electrochem. Commun.*, 2014, **47**, 80–83.
182 X. Zhang, J. Lei, D. Wu, X. Zhao, Y. Jing and Z. Zhou, *J. Mater. Chem. A*, 2016, **4**, 4871–4876.
183 X. Xie, S. Chen, W. Ding, Y. Nie and Z. Wei, *Chem. Commun.*, 2013, **49**, 10112–10114.
184 G. Zou, B. Liu, J. Guo, Q. Zhang, C. Fernandez and Q. Peng, *ACS Appl. Mater. Interfaces*, 2017, **9**, 7611–7618.
185 G. Gao, A. P. O'Mullane and A. Du, *ACS Catal.*, 2017, **7**, 494–500.
186 X. Li, G. Fan and C. Zeng, *Int. J. Hydrogen Energy*, 2014, **39**, 14927–14934.

 © 2023 The Author(s). Published by the Royal Society of Chemistry